

Cite this: *J. Mater. Chem. B*,
2024, 12, 6856

Microenvironment-responsive release of Mg²⁺ from tannic acid decorated and multilevel crosslinked hydrogels accelerates infected wound healing†

Na Li,^{abc} Yi Cao,^{ab} Jingyi Liu,^{ab} Wen Zou,^{abc} Manyu Chen,^{ab} Hongfu Cao,^{ab}
Siyan Deng,^{ab} Jie Liang,^{abc} Tun Yuan,^{id abc} Qiguang Wang,^{id *ab} Yujiang Fan^{id *ab}
and Xingdong Zhang^{ab}

The management of chronic infected wounds poses significant challenges due to frequent bacterial infections, high concentrations of reactive oxygen species, abnormal immune regulation, and impaired angiogenesis. This study introduces a novel, microenvironment-responsive, dual dynamic, and covalently bonded hydrogel, termed OHA-P-TA/G/Mg²⁺. It is derived from the reaction of tannic acid (TA) with phenylboronic acids (PBA), which are grafted onto oxidized hyaluronic acid (OHA-P-TA), combined with GelMA (G) via a Schiff base and chemical bonds, along with the incorporation of Mg²⁺. This hydrogel exhibits pH and ROS dual-responsiveness, demonstrating effective antibacterial capacity, antioxidant ability, and the anti-inflammatory ability under distinct acidic and oxidative microenvironments. Furthermore, the release of Mg²⁺ from the TA–Mg²⁺ network (TA@Mg²⁺) promotes the transformation of pro-inflammatory M1 phenotype macrophages to anti-inflammatory M2 phenotype, showing a microenvironment-responsive response. Finally, *in vivo* results indicate that the OHA-P-TA/G/Mg²⁺ hydrogel enhances epithelial regeneration, collagen deposition, and neovascularization, showing great potential as an effective dressing for infected wound repair.

Received 9th May 2024,
Accepted 8th June 2024

DOI: 10.1039/d4tb01000k

rsc.li/materials-b

1. Introduction

The treatment of infected wounds presents a great clinical challenge due to their high localized bacterial colonization.^{1,2} Bacteria discharge a variety of substances that can instigate an intense and extended inflammatory response, undermine the extracellular matrix (ECM) in host tissues shortly after colonization and infection, and drastically impede the wound healing process. Inflammatory cells induced at the wound site generate large amounts of reactive oxygen species (ROS), leading to apoptosis and vascular damage, thereby inducing oxidative stress and prolonged inflammation.^{1,3,4} Moreover, the persistent inflammatory response further worsens the immune microenvironment of wound healing through the secretion of

a large number of inflammatory factors, interrupting the transition of the wound healing process from the inflammatory phase to the proliferative phase.^{5,6} Therefore, therapeutic strategies such as antioxidants, antimicrobials, anti-inflammatories, and vascular regeneration can be used for the resolution of infected wounds to re-establish microenvironmental balance.

The standard approach to treating bacterial infections involves the use of antibiotics. However, the misuse of antibiotics has contributed to a crisis of drug resistance and often fails to address the comprehensive needs of the healing process for infected wounds.⁶ The advent of hydrogels has introduced novel strategies for the treatment of infected wounds. Hydrogels, characterized by their soft, three-dimensional network structures, serve as multifunctional dressings that maintain a moist microenvironment, facilitate the passage of water and oxygen, absorb excess exudates, and provide protection against microorganisms. Injectable self-adaptive hydrogels, known for their responsiveness to stimuli, are capable of adapting intelligently to changes in the wound's microenvironment, including temperature, pH, and humidity.⁷ The functional properties of injectability and self-healing are realized through reversible physical noncovalent interactions and chemical covalent

^a National Engineering Research Center for Biomaterials, Sichuan University, 29# Wangjiang Road, Chengdu, Sichuan, 610064, China.

E-mail: fan_yujiang@scu.edu.cn, wqgwang@126.com

^b College of Biomedical Engineering, Sichuan University, 29# Wangjiang Road, Chengdu, Sichuan 610064, China

^c Sichuan Testing Center for Biomaterials and Medical Devices, Sichuan University, 29# Wangjiang Road, Chengdu 610064, China

† Electronic supplementary information (ESI) available. See DOI: <https://doi.org/10.1039/d4tb01000k>

bonding mechanisms such as a Schiff base, a boronic acid–diol complex, disulfide bonds, and metal–ligand coordination. Among these, the methacrylate gelatin (GelMA) hydrogel is noted for its superior biocompatibility and versatility, which encompass mechanical, swelling, degradation, and biological characteristics, with a notable capacity to carry bioactive substances.^{8,9} The arginine–glycine–aspartic acid (RGD) peptide sequence within the hydrogel can stimulate cell adhesion and platelet activation, potentially endowing the hydrogel with superior cell adhesion properties and the capability to promote hemostasis. However, GelMA as a skin dressing is still limited by its rapid degradation, inadequate mechanical properties, and limited functionality.⁹ Hyaluronic acid (HA), a key component of the extracellular matrix, is essential for various physiological processes, including joint lubrication, blood vessel wall permeability regulation, protein and electrolyte diffusion management, and wound healing facilitation. Despite these advantages, HA's use as a standalone wound repair material is restricted due to its inferior mechanical properties, lack of adhesion, excessive swelling, and early degradation. However, these limitations can be overcome by chemically modifying HA, which involves oxidizing its *o*-diol structure into dialdehyde and forming chemical bonds through cross-linking with other polymers.^{10,11}

The treatment of incorporating cytokines, cells, and drugs into hydrogels has issues with incomplete release, high cost, and does not account for changes in the microenvironment during the healing process. Intrinsically antioxidant hydrogels prepared by grafting antioxidant units onto polymer chains, such as dopamine, gallic acid, eugenol, cysteine, and phenylboronic ester, can be utilized to eliminate free radicals. Tannic acid (TA), a typical hydrolysable tannin abundant in fruits and plants, is a polyphenolic compound containing numerous catechol and gallol groups. It has the ability to bind proteins and functions as an antioxidant, anti-inflammatory, and antimicrobial agent.^{12,13} Phenylboronic acids (PBA) have the ability to establish reversible covalent boronic ester bonds with diols when the pH level is equal to or exceeds their pK_a value (7.8). These reactions can be used to target the response and release of specific molecules in specific environments. Furthermore, these boronic ester bonds exhibit high sensitivity to ROS under oxidative conditions. The combination of polyphenols with hydrogels grafted with phenylboric acid through chemical bonding endows hydrogels not only with injectable self-healing ability, pH/ROS response release, and scavenging ability but also with inherent antioxidant ability.^{14,15} Magnesium ions (Mg^{2+}), essential elements for biological growth and development and various enzyme agonists, have been shown to significantly enhance the antioxidant and antimicrobial properties, and other activities when complexed with amino acids or quercetin.¹⁶ However, the specific mechanism remains unclear. It has been demonstrated that incorporating Mg^{2+} into a hydrogel promotes cell proliferation, differentiation, and tissue regeneration. However, the uncontrolled release of Mg^{2+} limits the application. TA can form stable complexes with various metal ions such as Mn^{2+} , Fe^{3+} , and Cu^{2+} , enhancing its

structural stability and regulating the microenvironment to increase its effectiveness.^{4,7} Thus the smart hydrogel now possesses the capability of modifying its own structure, responding to the release of functional substances, and adapting to changes in the microenvironment of the infected wound.

In this study, we aimed to develop a dual dynamic covalently bonded hydrogel incorporating Mg^{2+} (OHA-P-TA/G/ Mg^{2+}). This hydrogel has a multilevel crosslinked structure that is derived from the reaction of TA with a PBA graft onto oxidized hyaluronic acid (OHA-P-TA), combined with GelMA (G) *via* a Schiff base and chemical bonds. The OHA-P-TA/G/ Mg^{2+} hydrogel, possessing a multitude of features such as the self-healing ability, injectability, antibacterial properties, and pH/ROS dual-responsive attributes, was engineered to facilitate the controlled release of TA and Mg^{2+} in a spatiotemporal manner. It has the potential to suppress the inflammatory response and expedite the healing process in infected wounds. As shown in Fig. 1, phenylboronic acid-grafted oxidized dextran (POD) and amidogen of G form the primary network structure, and the hydroxyl group on the TA, along with PBA grafted onto oxidized hyaluronic acid, forms chemical bonds for achieving pH/ROS response. Meanwhile, the secondary structure is composed of G by photo-crosslinking.¹⁷ In addition to further enhancing the stability of the hydrogel structure, Mg^{2+} chelated with TA is slowly released in the hydrogel system and spatially and temporally responds to the wound microenvironment, synergistically playing a role in promoting wound healing.¹⁵ The pH/ROS dual-responsive attributes of the hydrogel originate from the structure of boronic ester bonds and Schiff base breakage. In addition, a comprehensive evaluation was conducted on the physical attributes, release characteristics, antibacterial efficacy, and biocompatibility. The healing efficacy of the hydrogel dressing was assessed in a model involving a full-thickness skin defect and infection.

2. Materials and methods

2.1 Materials

Sodium hyaluronate (HA, viscosity-average molecular weight of 1.20×10^6) was procured from Bloomage Freda Biopharm Co., Ltd, China. Methacrylic anhydride (MA) was supplied by Sinopharm Chemical Reagent Co., Ltd, China. *N*-Hydroxysuccinimide (NHS) was sourced from Shanghai Aladdin Biochemical Technology Co., Ltd. 1-Ethyl-3-(3-dimethylaminopropyl) carbodiimide hydrochloride (EDC-HCl) was obtained from Shanghai Medpep Co., Ltd. Tannic Acid (TA) and gelatin were provided by Sigma-Aldrich, USA. Lithium phenyl(2,4,6-trimethylbenzoyl)phosphinate (LAP) was bought from Shanghai Maclean Biochemical Technology Co., Ltd. 3-Aminophenylboronic acid (PBA) was procured from Shanghai Aladdin Industrial Co., Ltd. Phosphate buffered saline (PBS) was bought from Invitrogen. Dulbecco's Modified Eagle Medium (DMEM), fetal bovine serum (FBS), and penicillin/streptomycin (PS) were sourced from Gibco (USA). Mouse fibroblasts (L929) cells were purchased from Procell Life Science & Technology Co., Ltd (Wuhan, China). All other reagents were of analytical grade.

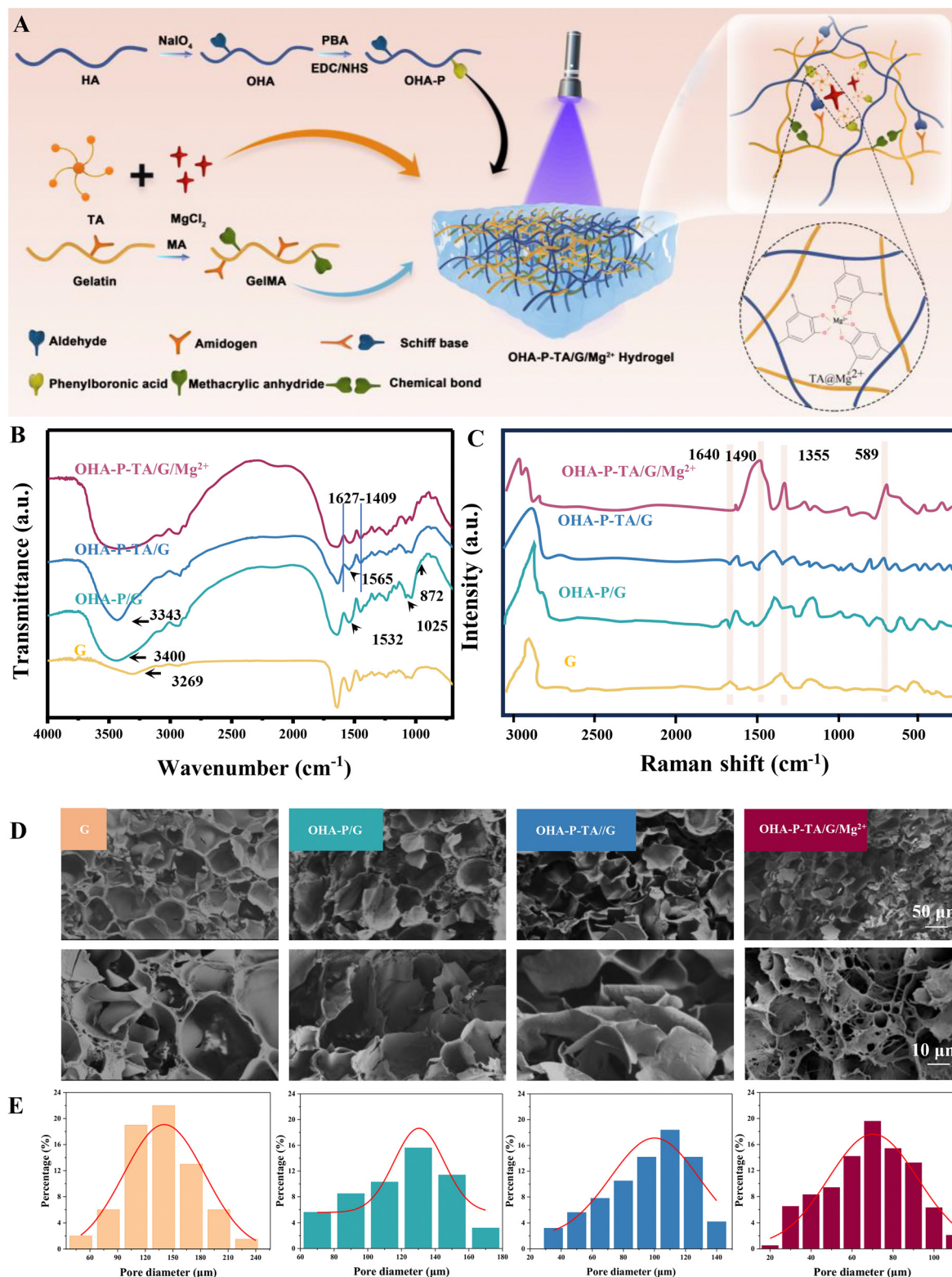


Fig. 1 Preparation and characterization of G, OHA-P/G, OHA-P-TA/G and OHA-P-TA/G/Mg²⁺ hydrogels. (A) Schematic diagram of the OHA-P-TA/G/Mg²⁺ hydrogel synthesis scheme. (B) FTIR spectra of the G, OHA-P/G, OHA-P-TA/G and OHA-P-TA/G/Mg²⁺ hydrogels. (C) Raman spectra of hydrogels. (D) SEM images of various dry hydrogels. (E) Distribution of pore size for different hydrogels, respectively. Data are shown as mean \pm SD, $n = 3$. * $p < 0.05$, ** $p < 0.01$, *** $p < 0.001$, **** $p < 0.0001$.

2.2 Synthesis of OHA, OHA-PBA (OHA-P), and GelMA (G)

A solution of hyaluronic acid (0.8% w/v, dissolved in 15 mL of deionized water) was mixed with NaIO₄ (2.14 g) and stirred for 2 h in a dark environment at room temperature. Ethylene glycol (5 mL) was then introduced to neutralize any remaining NaIO₄ over a period of 2 h. Following a 3-day dialysis process using a dialysis membrane (MWCO-3500 Da), the product was subjected to freeze-drying to obtain OHA. The process of conjugating PBA to OHA involved amidation. In this process, OHA (0.6 g) was dissolved in 200 mL of DI water. EDC (0.37 g) and NHS (0.4 g) were added to the solution and stirred for 30 min to activate the carboxyl groups of OHA. Subsequently, 3-aminophenylboronic acid (0.123 g, 0.900 mmol) was introduced to the mixture and stirred for 24 h. The reaction solution underwent thorough dialysis against deionized water for 3 days. Ultimately, OHA-P was produced using lyophilization with a cold trap set at $-80\text{ }^{\circ}\text{C}$ and a vacuum of 1 Pa, and its characteristics were determined by ¹H NMR. Gelatin was dissolved in PBS at $50\text{ }^{\circ}\text{C}$ (10% w/v). MA (8 mL) was slowly added to react with continuous stirring for 2 h, and the reaction was terminated by adding an equal volume of alkaline solution. The reaction solution was dialyzed extensively against DI water for 5 days at a temperature of $50\text{ }^{\circ}\text{C}$. GelMA was finally obtained through lyophilization and its properties were analyzed using ¹H NMR.

2.3 Preparation of OHA-P-TA/G/Mg²⁺ hydrogels

LAP, serving as a catalyst for the photo-crosslinking reactions of methacrylate groups, was dissolved in PBS at a concentration of 0.3% (w/v) and heated to $50\text{ }^{\circ}\text{C}$ for a duration of 15 min. To optimize the concentration of OHA-P and TA, concentration gradients of OHA-P and TA were added, and the cell viability was evaluated. Compared with other groups, a combination of 2% OHA-P and G exhibited the best cell viability. UV light was applied for 10 s to quickly solidify the mixture.

Subsequently, OHA-P powder was dissolved in LAP solution with concentrations of 2% (w/v) and heated to $50\text{ }^{\circ}\text{C}$ for 1 h. After that, GelMA was introduced to the PBS solution and stirred continuously for 2 h, resulting in a final GelMA concentration of 8% (w/v). TA was then dissolved in the aforementioned solution at varying concentrations, with C (TA) = $5000\text{ }\mu\text{g mL}^{-1}$, which was selected based on the cytotoxicity and the optimal compression modulus. 0.5% MgCl₂ was added as a reference to the previous research in our laboratory. Finally, the composite solution was injected into molds and exposed to 405 nm light for 60 s to facilitate cross-linking. The GelMA, OHA-P/GelMA, OHA-P-TA5000/GelMA, and OHA-P-TA5000/GelMA/0.5% MgCl₂ hydrogels were named G, OHA-P/G, OHA-P-TA/G, and OHA-TA/G/Mg²⁺ respectively.

2.4 Physicochemical analysis

The physical and chemical characteristics of hydrogels were investigated *via* nuclear magnetic resonance (¹H NMR), UV-vis spectroscopy, Fourier transformed infrared spectroscopy (ATR-FTIR), Raman microscopy, scanning electron microscopy

(SEM), X-ray photoelectron spectroscopy (XPS), X-ray diffraction (XRD), thermal gravimetric analysis (TG), differential scanning calorimetry (DSC), and dynamic mechanical analysis (DMA), and using the swelling ratio, and *in vitro* degradability. The detailed methods are presented in the ESI.†

2.5 Rheological analysis

The rheological properties of the disk-shaped hydrogels (25 mm × 1 mm) were evaluated at ambient temperature using a rheometer (TA, HR20, USA). ESI† details the procedures for the rheological analysis.

2.6 Investigation of TA and Mg²⁺ release characteristics

The release of TA from the OHA-TA/G/Mg²⁺ hydrogel was quantified using UV-vis spectroscopy following a previously described method.¹⁸ Disk-shaped hydrogels were immersed in 5 ml of various solutions (pH 7.4 and 4.5) and H₂O₂ (1 mM) to study the TA release. The quantity of Mg²⁺ released was ascertained using inductively coupled plasma-mass spectrometry (ICP-MS).¹⁹

2.7 Evaluation of *in vitro* antioxidant capability

The antioxidant abilities of the hydrogels were assessed using a fluorometric intracellular ROS Kit and ABTS radical scavenging and DPPH radical scavenging activity in previous research. ESI† details the methods.

2.8 Evaluation of antibacterial properties

The antibacterial properties of each hydrogel were assessed using *Escherichia coli* (*E. coli*, ATCC 25922) and *Staphylococcus aureus* (*S. aureus*, ATCC 25923). The agar diffusion assay was employed to measure the antibacterial ability in the surface diffusion of the hydrogel by analyzing the zone of inhibition (ZOI). ESI† details the methods.

2.9 *In vitro* cell experiments

The direct and indirect cytocompatibility of the hydrogels was assessed through FDA/PI staining and the cell counting Kit-8 (CCK-8). Cell migration and tube formation assays were employed to evaluate the hydrogels' effects on cell proliferation, migration, and angiogenesis. The detailed methods of the above tests are documented in the ESI.†

RAW 264.7 macrophages were incubated for 12 h in DMEM containing lipopolysaccharide (LPS, $1\text{ }\mu\text{g mL}^{-1}$), after which they were incubated with various hydrogels. The intracellular level of NO was detected by DAF-FM DA. The treated cells were then stained with FITC-tagged anti-CD86 antibodies and APC-tagged CD206 following the instructions provided by the manufacturer, and subsequently analyzed using flow cytometry. Quantitative real-time PCR was used to ascertain the mRNA expression. The sequences of the primers are provided in Table S1 (ESI†). The detailed methods of the above tests are documented in the ESI.†

2.10 *In vivo* wound healing

The animal study received approval from Sichuan University's Medical Ethics Committee (KS2022330). Male BALB/c mice, weighing around $25 \text{ g} \pm 5 \text{ g}$ and aged between 6 and 8 weeks, were obtained from Vital River Laboratory Animal Technology Co., Ltd (Beijing, China). Before creating an infected wound, the mice were anesthetized using intraperitoneal injections of chloral hydrate (0.5 mg kg^{-1}), and a full-thickness skin wound with a diameter of 10 mm. Subsequently, $100 \mu\text{L}$ of *S. aureus* (10^8 CFU mL^{-1}) was administered to the defect wound to induce infection for 1 day. On day 2, infected tissue samples were gathered and meticulously mixed with 2 mL of TSB in a sterile environment for an *in vivo* antibacterial ability test. The detailed methods of the above tests are documented in the ESI†

2.11 Histologic analysis

The process of epidermal regeneration in wound tissues was evaluated using various staining techniques, including hematoxylin and eosin (H&E), Masson's trichrome, Sirius red staining, and immunohistochemical staining. The detailed methods are presented in the ESI†

2.12 Statistical analysis

Statistical analysis was conducted using SPSS 25.0 software. The data collected were represented as the mean \pm standard deviation from three distinct experiments. Data analysis was performed using the GraphPad Prism software (GraphPad Software Inc.) and involved statistical tests such as the Student's *t*-test (unpaired and two-tailed), one-way or two-way ANOVA, supplemented by a Tukey *post hoc* test. When $p < 0.05$ (*), $p < 0.01$ (**), $p < 0.001$ (***), and $p < 0.0001$ (****), the difference was considered significant.

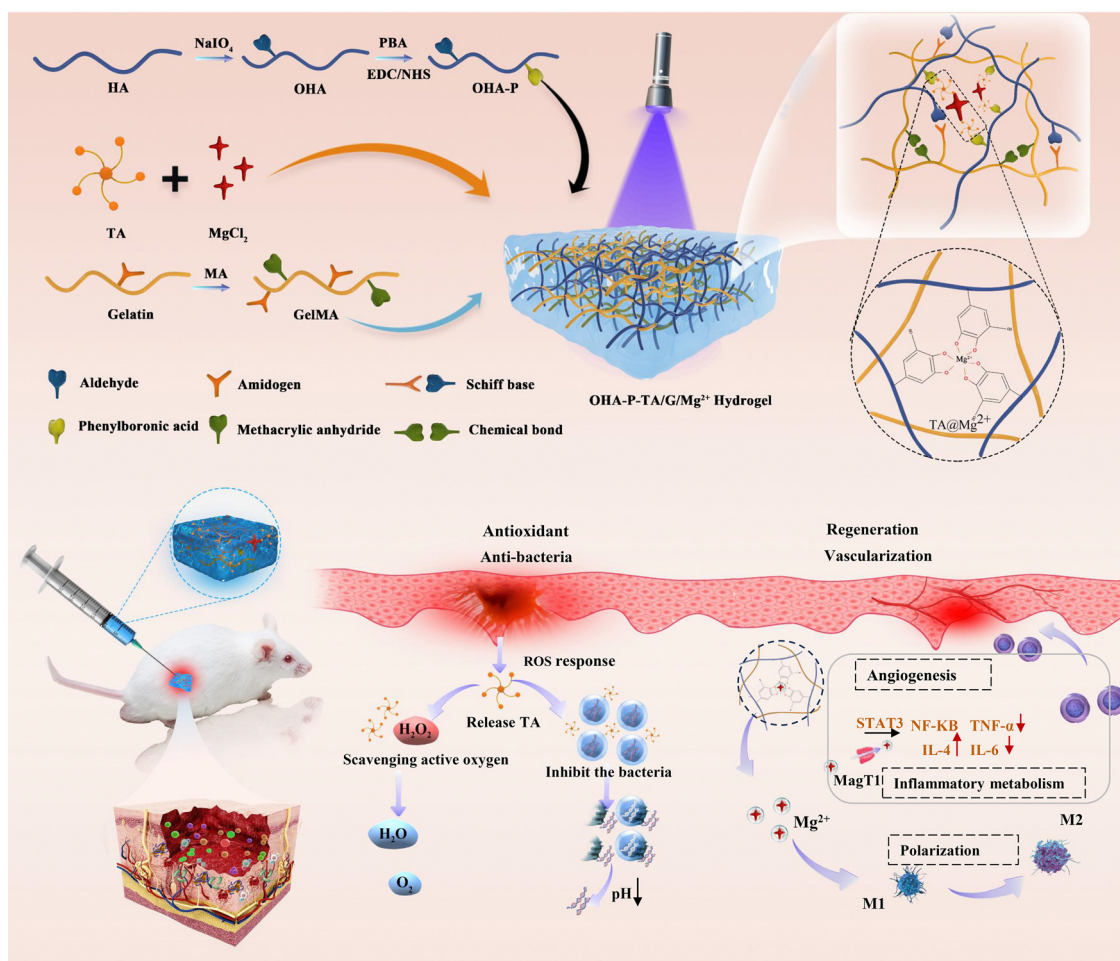
3. Results and discussion

3.1 Preparation and characterization of the OHA-P-TA/G/Mg²⁺ hydrogel

To address the multifaceted needs of chronic wound healing, a self-healing, tissue-adhesive, antioxidant, anti-inflammatory hydrogel loaded with OHA-P, G, TA, and Mg²⁺ was designed. This double crosslinked hydrogel aims to meet the complex requirements of treating chronic infected wounds. The synthesis diagram of the hydrogel is presented in Fig. 1(A). HA was chosen as the primary network molecule due to its excellent biocompatibility and metal coordination properties. Sodium periodate was utilized to yield oxidized HA (OHA) (Fig. S1A, ESI†). The ¹H NMR spectra result revealed new proton signals at 4.90, 5.00, and 5.10 ppm (1, 2, and 3, respectively), which correspond to the hemiacetalic proton formed from aldehydes and neighboring hydroxyl groups (Fig. S2A, ESI†). The degree of oxidation is approximately 42.10%. PBA was grafted onto the aldehyde groups of the OHA chain through a Schiff base reaction by classical EDC/NHS chemistry to synthesize phenylboronic acid-grafted oxidized hyaluronic acid (OHA-P) (Fig. S1B and S2A, ESI†). The ¹H NMR spectra showed proton-specific

signals for phenylboronic acid at 7.3 to 7.7 ppm (4, 5, 6, and 7, respectively), and the substitution degree of PBA was quantified to be approximately 38.7% by comparing the peak area of these proton-specific signals in each group to that of a methyl group (δ 1.90) (Fig. S1A, ESI†).²⁰ FTIR spectra showed that the peak at 1730 cm^{-1} represents the stretching vibration of the $\text{C}=\text{O}$ of the aldehyde group, contributed by the oxidation of sodium periodate.²¹ Compared to OHA, the OHA-P polymer spectrum displayed a new peak at 1459 cm^{-1} and 1517 cm^{-1} which was attributed to the benzene ring. Moreover, new peaks emerged at 1340 cm^{-1} and 700 cm^{-1} , which were ascribed to the tensile vibration of $\text{B}-\text{O}$ and the bending vibration of $\text{C}-\text{H}$ in phenylboronic acid, respectively (Fig. S2B, ESI†). The results confirmed the successful oxidization to OHA and conjugation of phenylboronic acid groups onto OHA (Scheme 1).

To introduce Schiff base bonds and photo-crosslinking chemical bonds into the hydrogel network, MA-modified gelatin was chosen as an additional primary component (Fig. S1C, ESI†). The FTIR spectra of the OHA-P/G hydrogel revealed the distinctive peaks of pyranoses (1025 cm^{-1}) and mannose (872 cm^{-1} and 802 cm^{-1}), signifying the incorporation of OHA-P into the composite G hydrogel (Fig. 1(B)). The spectra indicated the creation of $\text{C}=\text{N}$ ($1690\text{--}1590 \text{ cm}^{-1}$). Additionally, the peak around 3400 m^{-1} intensified, corresponding to OH and NH_2 stretching vibrations (Fig. 1(B)), implying an interaction between NH_2 groups (GelMA) and $\text{C}=\text{O}$ groups (OHA-P). TA, which contains numerous aromatic rings, exhibits an absorption peak at 270–320 nm, whereas OHA-P does not. As depicted in Fig. S2C (ESI†), absorption peaks at 270–280 nm are present in TA and OHA-P-TA, suggesting that TA was integrated into OHA-P (Fig. S2C, ESI†).²² After the addition of TA, the FTIR demonstrated that OHA-P-TA had multiple peaks at 1627 cm^{-1} and 409 cm^{-1} attributable to the aromatic rings. Furthermore, the infrared peaks of the $\text{B}-\text{O}-\text{C}$ formed by the reaction of the *O*-dihydroxyl group of TA with PBA are mainly concentrated in the region of $1200\text{--}1600 \text{ cm}^{-1}$, with the most significant peak at 1370 cm^{-1} , which corresponds to the $\text{C}-\text{O}$ stretching vibration frequency of the borate bond. The peak at 1565 cm^{-1} , corresponding to $\text{C}-\text{C}$ stretching for the aromatic ring, indicated the successful conjugation of OHA-P with TA. The FTIR spectra revealed a shift in the peak from approximately 3343 cm^{-1} , which corresponds to the OH stretching vibration, to a lower wavenumber of 3400 cm^{-1} . This shift, which also resulted in a broader peak, indicates the constitution of H-bonds between TA, OHA-P, and G. Upon adding Mg²⁺, the peak at about 3343 cm^{-1} broadened, suggesting the formation of a TA@Mg²⁺ network. The Raman spectra showed a typical characteristic band of $\text{C}=\text{C}$ in GelMA at about 1600 cm^{-1} . Furthermore, the Raman spectra of OHA-P-TA/G and OHA-P/G showed the sharply decreased intensity of $1600\text{--}1640 \text{ cm}^{-1}$ bands implying the polymerization of $\text{C}=\text{C}$ in the G hydrogel. Moreover, OHA-P-TA/G/Mg²⁺ showed new peaks around 540 cm^{-1} , 1357 cm^{-1} , and 1450 cm^{-1} , which was assigned to the vibration of Mg-O bonds formed by the chelation of Mg²⁺ with a phenolic hydroxyl group (Fig. 1(B)). The XPS results confirmed the effective incorporation of Mg²⁺ within the hydrogel. The binding energy of $\text{C}-\text{C}$, $\text{C}-\text{B}$, $\text{C}=\text{C}$, $\text{C}-\text{N}$ and $\text{C}-\text{O}$ in the OHA-P-TA/G/Mg²⁺ suggested that the hydrogel may also have multiple



Scheme 1 Schematic illustration of the microenvironment-responsive release of TA and Mg²⁺ from OHA-P-TA/G/Mg²⁺ hydrogels to enhance infected wound healing.

bonds interacting within the matrix, and Mg²⁺ was introduced to coordinate with TA (Fig. S3A, ESI[†]). Additionally, TG and DSC analyses of OHA-P-TA/G/Mg²⁺ were conducted to assess the chemical stability. Both TG and DSC analyses indicated that the stability of OHA-P-TA/G/Mg²⁺ was maintained until the temperature surpassed 310 °C, as depicted in Fig. S3B (ESI[†]). The wide-scan XPS spectrum of the OHA-P-TA/G/Mg²⁺ hydrogel was analyzed (as shown in Fig. S3C, ESI[†]). The analysis indicated that the primary chemical components of the gel were organic elements such as C, O, N, B, and Mg. In summary, the major network of the OHA-P-TA/G/Mg²⁺ hydrogel is composed of multiple crosslinking by photo-induced polymerization, H-bond interactions and Schiff base bonds formed through chemical reactions (Fig. 1(A)).

The pore size and structure in a tissue engineering scaffold play a vital role in influencing the cell viability, attachment, and differentiation. Fig. 1(D) illustrates the typical microstructure of hydrogels. Each of the hydrogels displayed a consistent and interlinked 3D porous structure. The pore size of the double crosslinked OHA-P/G hydrogel ($100.10 \pm 3.96 \mu\text{m}$) was found to be smaller than that of the single network G hydrogel ($130.44 \pm 3.95 \mu\text{m}$). The OHA-P-TA/G hydrogel ($95.30 \pm 6.64 \mu\text{m}$) was characterized by multiple hydrogen bonds between OHA-P and

G. The addition of TA resulted in a denser pore structure, primarily due to the intermolecular H-bonds between OHA-P and G. The OHA-P-TA/G/Mg²⁺ hydrogel, with a pore size of $65.77 \pm 0.71 \mu\text{m}$, exhibited a smaller pore size than the OHA-P-TA/G hydrogel. This was attributed to the complex chelation between Mg²⁺ and TA (Fig. 1(E)). Energy dispersive spectroscopy (EDS) elemental mapping (Fig. S4A, ESI[†]) and spectra (Fig. S4B, ESI[†]) confirmed the uniform distribution of the elements C, O, and Mg in the OHA-P-TA/G/Mg²⁺ hydrogel, whereas the OHA-P-TA/G hydrogel contained only the elements C and O. The crystal structure was analyzed using XRD (Fig. S4C, ESI[†]) and the results showed that OHA-P-TA/G/Mg²⁺ has higher crystallinity than OHA-P-TA/G and OHA-P/G. This is consistent with the SEM observations, which revealed a large number of small voids and numerous crystals in the void wall.

3.2 Mechanical properties, rheological properties, swelling ratios, and *in vitro* degradation behavior of the hydrogels

The rapid gelation, viscoelasticity, mechanical properties, injectability, self-healing ability and swelling properties of hydrogel dressings are critical for its application in dynamic skin wounds. The ability to gel quickly is crucial in hemostasis,

as it enables the swift sealing of damaged tissues, especially at sites of bleeding wounds. The gelation process of the hydrogels showed a transition from a liquid state to a solid state, as shown in Fig. 2(A). The gelling kinetics of the hydrogels were observed using a rheometer during a time sweep conducted under UV light. With exposure to UV light, G' rose swiftly, surpassing G'' and stabilizing within 60 s (as shown in Fig. 2(B)). Importantly, the moment when G' was equal to G'' and G'' of the OHA-P-TA/G/Mg²⁺ hydrogel were higher than those of the G, OHA-P/G, and OHA-P-TA/G solutions. In

addition, the G' of all hydrogels is always higher than G'' in the frequency sweep range from 0.1 to 10 Hz, which could show the stable structure and the elasticity of hydrogels. However, both G' and G'' slightly increased after incorporating TA and Mg²⁺ into the OHA-P/G hydrogels. All hydrogels exhibited a storage modulus (G') that was approximately ten times higher than their loss modulus (G''). Moreover, both G' and G'' of the OHA-P-TA/G/Mg²⁺ hydrogel were higher than those of the G, OHA-P/G, and OHA-P-TA/G hydrogels (Fig. 2(C)).

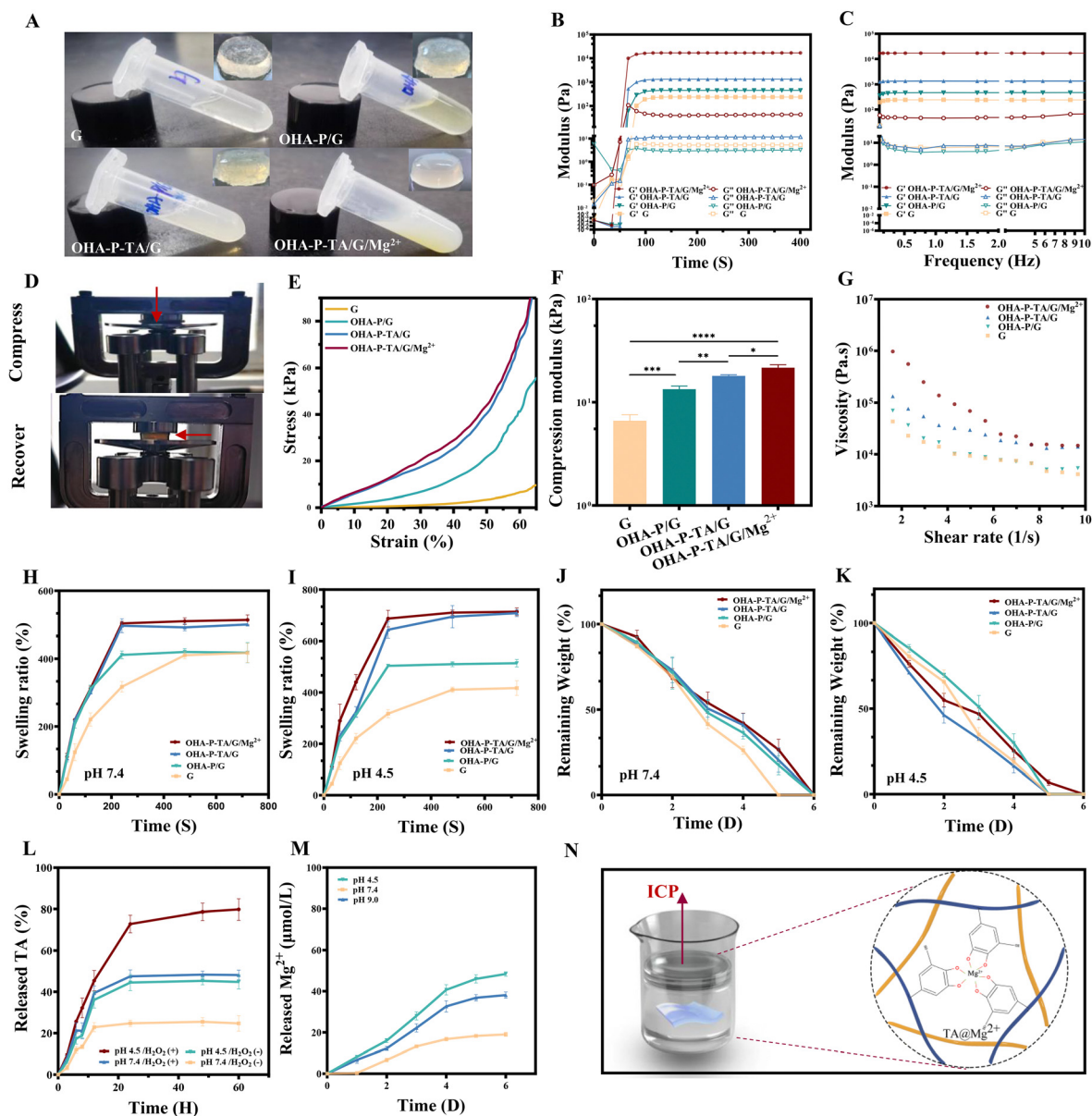


Fig. 2 Characterization of physical and chemical properties of the hydrogels. (A) Images of the preparation process of hydrogels from liquid to gel. (B) The storage modulus (G') and loss modulus (G'') of hydrogels change with time. (C) Frequency sweep test of hydrogels. (D) Compression and recovery process diagram. (E) Compression stress–strain curves for different hydrogels. (F) Maximum Compressive stress of different hydrogels. (G) The viscosity of hydrogels changes with shear rate. (H) and (I) Swelling ratio of various dry hydrogels at pH 7.4 and 4.5. (J) and (K) Remaining weight of various dry hydrogels at pH 7.4 and 4.5. (L) Release kinetics of TA from the OHA-P-TA/G/Mg²⁺ hydrogel under different conditions. (M) and (N) The released Mg²⁺ from OHA-P-TA/G/Mg²⁺ hydrogel under different conditions by ICP. Data are shown as mean \pm SD, $n = 3$. * $p < 0.05$, ** $p < 0.01$, *** $p < 0.001$, **** $p < 0.0001$.

Fig. 2(D) shows the DMA compression test of hydrogels. As depicted in Fig. 2(E), the stress–strain curve demonstrated an enhancement in stiffness with an increase in cross-linking and the inclusion of TA. The compression modulus of the OHA-P-TA/G/Mg²⁺ hydrogel (21.66 ± 8.24 kPa) was significantly higher than that of the individual component G (6.60 ± 1.84 kPa) and the double crosslinked OHA-P/G (13.39 ± 4.43 kPa) (refer to Fig. 2(F)). A dual-crosslinked hydrogel structure exhibits superior mechanical characteristics compared with a single network. The addition of TA and Mg²⁺ further increased the compression modulus of the double cross-linked network. The compression modulus obtained falls within the spectrum of physiological soft tissue, making it an ideal scaffold for facilitating cell proliferation, migration, and differentiation. Additionally, amplitude sweep tests revealed a linear viscoelastic region for all hydrogels, indicating the ability to maintain their form and exhibit suitable extensibility. All the hydrogels exhibited a shear-thinning behavior, with a decrease in viscosity as the shear rate increased, indicating their excellent shear-thinning ability. Among them, the OHA-P-TA/G/Mg²⁺ hydrogel demonstrated the best dynamic chemical bonding and structure integrity (Fig. 2(G)).

Specifically, the OHA-P-TA/G/Mg²⁺ hydrogel is capable of retaining a firm adherence to skin tissue. Due to their excellent flexibility, hydrogels can be utilized on the human wrist, allowing for unrestricted bending in tandem with joint movements (Fig. S5A, ESI[†]), and even when subjected to movement in a fluidic environment. Fig. S5C (ESI[†]) illustrates the excellent injectable properties of the hydrogel. As shown in Fig. S5D (ESI[†]), the internal structure of the OHA-P-TA/G/Mg²⁺ hydrogel collapsed under a strain of 760%, and an amplitude sweep of strain was conducted at 1% and 760% strains. Upon increasing the strain to 760%, G' rapidly decreased from approximately 800 to 10^{-4} Pa, becoming less than G'' , suggesting a viscous liquid-like behavior and indicating an impaired internal structure. In contrast, at a strain of 1%, G' and G'' returned to their initial values even after four repeated cycles, illustrating a solid-like elastic behavior and a reformed network. These results demonstrate that an injectable self-healing hydrogel with good mechanical properties is suitable for the application of skin wounds through chemical modification.

Given that bacterial-infected environments are typically weakly acidic and high in ROS, the swelling and degradation patterns of the fabricated hydrogels were examined under both neutral (pH 7.4) and acidic (pH 4.5) conditions. The Schiff-base reaction between OHA and G is reversible and transitions between acidic and alkaline microenvironments. The dynamic boronic acid ester formed by the reaction between TA and OHA-P is highly sensitive to ROS. As depicted in Fig. 2(H) and (I), the swelling profiles of all hydrogels were evaluated at pH 7.4 and 4.5. At pH 7.4, the G hydrogel achieved equilibrium after an immersion period of 480 s, whereas the OHA-P/G and OHA-P-TA/G hydrogels took only 240 s (Fig. 2(H)). G exhibited similar swelling behaviors at pH 4.5 (refer to Fig. 2(I)), including the time taken to reach swelling equilibrium and the equilibrium swelling ratio. The results suggested that structural changes

leading to smaller voids are more favorable for the uptake of exudate solutions. In addition, the hydrogels containing OHA-P (OHA-P/G and OHA-P-TA/G) exhibited a significantly reduced time to reach swelling equilibrium and a greater equilibrium swelling ratio compared to the G hydrogel at pH 7.4.

As depicted in Fig. 2(J) and (K), the degradation patterns of all hydrogels vary under different conditions. At a pH of 7.4, all three hydrogels experienced significant degradation within 6 days. The G hydrogel degraded much more rapidly than the OHA-P/G, OHA-P-TA/G, and OHA-P-TA/G/Mg²⁺ hydrogels. After 5 days, the G hydrogel was completely degraded, while the other hydrogels lost approximately 70% of their weight under the same conditions. The degradation of the hydrogel was prolonged due to the stabilization of the Schiff base between G and OHA-P at pH 7.4 (Fig. 2(J)). At a pH of 4.5, the G hydrogels exhibited a similar degradation profile, although the degradation rate within the first 5 days was faster than that in the PBS solution (pH 7.4). Under acidic conditions, the total degradation behavior of the OHA-P/G hydrogel accelerated. The stability of the dual network structure had a greater impact on the degradation behavior of OHA-P/G than pH. However, under acidic conditions, the degradation behavior of the OHA-P-TA/G hydrogel changed dramatically. The OHA-P-TA/G lost more than 60% of its weight within the first 2 days, followed by a relatively slow degradation over the next 3 days. The dynamic chemical bonds of OHA-P-TA/G responded to pH breakage under acidic conditions, further accelerating the degradation behavior (Fig. 2(K)). Moreover, the presence of Mg²⁺ was found to reduce the degradation behavior of the OHA-P-TA/G hydrogel to a certain extent. Both the OHA-P-TA/G and OHA-P-TA/G/Mg²⁺ hydrogels could be progressively degraded and were almost completely degraded in 6 days. This indicates their good biodegradable properties, making them considerably suitable for hemostasis.

3.3 pH/ROS dual responsive behavior and TA and Mg²⁺ release of the hydrogels

Leveraging the dynamic Schiff base and boronic ester bonds, the OHA-P-TA/G hydrogel demonstrated responsive behavior under varying pH and redox conditions. As illustrated in Fig. 2(L), 43.62% of the TA was released from the hydrogel after 24 h of incubation under acidic conditions (pH 4.5) and 21.32% of the TA was released under neutral conditions (pH 7.4). Furthermore, when the solution contained 1 mM H₂O₂, the TA release rate reached 78.5% under acidic conditions (pH 4.5), and 45.32% under neutral conditions (pH 7.4), highlighting the high sensitivity of the Schiff base to pH and the boronic ester to ROS. The release profiles of Mg²⁺ from OHA-P-TA/G/Mg²⁺ were studied (Fig. 2(M) and (N)), when immersed under different conditions (pH 4.5, pH 7.4, and pH 9.0). Concurrently, the quantity of free Mg²⁺ produced under acidic conditions (pH 4.5) was 4.52 times greater than in the PBS solution (pH 7.4). The amount of Mg²⁺ produced under alkaline conditions (pH 9.0) was a little lower than under acidic conditions (pH 4.5). This result suggests that the magnesium ion release profile is closely related to the hydrogel's structure under different pH

conditions. As the bacteria are destroyed by TA, the pH of the infectious environment becomes acidic, leading to the further disintegration of the hydrogel structure. This disintegration is beneficial for releasing a large amount of Mg^{2+} , which in turn further promotes the antibacterial effect. The generation of TA and free Mg^{2+} led to the hypothesis that the chemical and chelating bonds in the hydrogel structure break down further under acidic conditions.²³ These findings indicated that the synthesized OHA-P-TA/G/ Mg^{2+} hydrogel exhibited properties of spatiotemporal delivery. It demonstrated a more efficient release pattern under an environment rich in acidity and ROS, which is advantageous for the treatment of persistently infected wounds.

3.4 Enhanced antioxidant and antibacterial effects *in vitro*

Excessive ROS and persistent bacterial infection can negatively impact the process of wound healing and tissue regeneration by provoking intense inflammation and setting off detrimental processes. Oxidative stress, often triggered by free radicals, is a common occurrence in wound healing and tissue regeneration by inducing severe inflammation and initiating harmful processes. Oxidative stress, often triggered by free radicals, is a common occurrence in wounds and has the potential to harm adjacent tissue cells, thereby extending the duration of wound

healing. A decrease in the local pH and a persistent inflammatory response can result from metabolic substances produced by bacterial infection. Hydrogel dressings, with their robust ROS scavenging and antibacterial abilities, can positively contribute to chronic wound healing (Fig. 3(A)).²⁴ To evaluate the therapeutic effect of the hydrogel as a potential ROS scavenging platform, the intracellular ROS levels of L929 cells (cultured with or without hydrogels) were detected by DCFH-DA staining in response to H_2O_2 (100 μM) stimulation. Illustrative images showcased that the utilization of OHA-P-TA/G, and OHA-P-TA/G/ Mg^{2+} hydrogel extracts noticeably decreased the ROS levels (Fig. 3(B)). It can be inferred from Fig. 3(C) that intracellular ROS levels were quantified by mean fluorescence intensity. The OHA-P-TA/G and OHA-P-TA/G/ Mg^{2+} extracts led to the most significant reduction in ROS. Additionally, the antioxidative activity of G, OHA-P/G, OHA-P-TA/G, and OHA-P-TA/G/ Mg^{2+} hydrogels was evaluated by the scavenging tests of ABTS radicals and DPPH radicals.²⁵ As shown in Fig. 3(D), all hydrogels containing TA displayed strong scavenging efficiency against DPPH radicals (>85%) when the concentrate was up to 3 mg mL⁻¹. Meanwhile, the TA-modified hydrogels showed strong scavenging efficiency against ABTS+ radicals (>90%), which implies that the antioxidant capacity of hydrogels is mainly from TA, and Mg^{2+} had a slight promoting effect

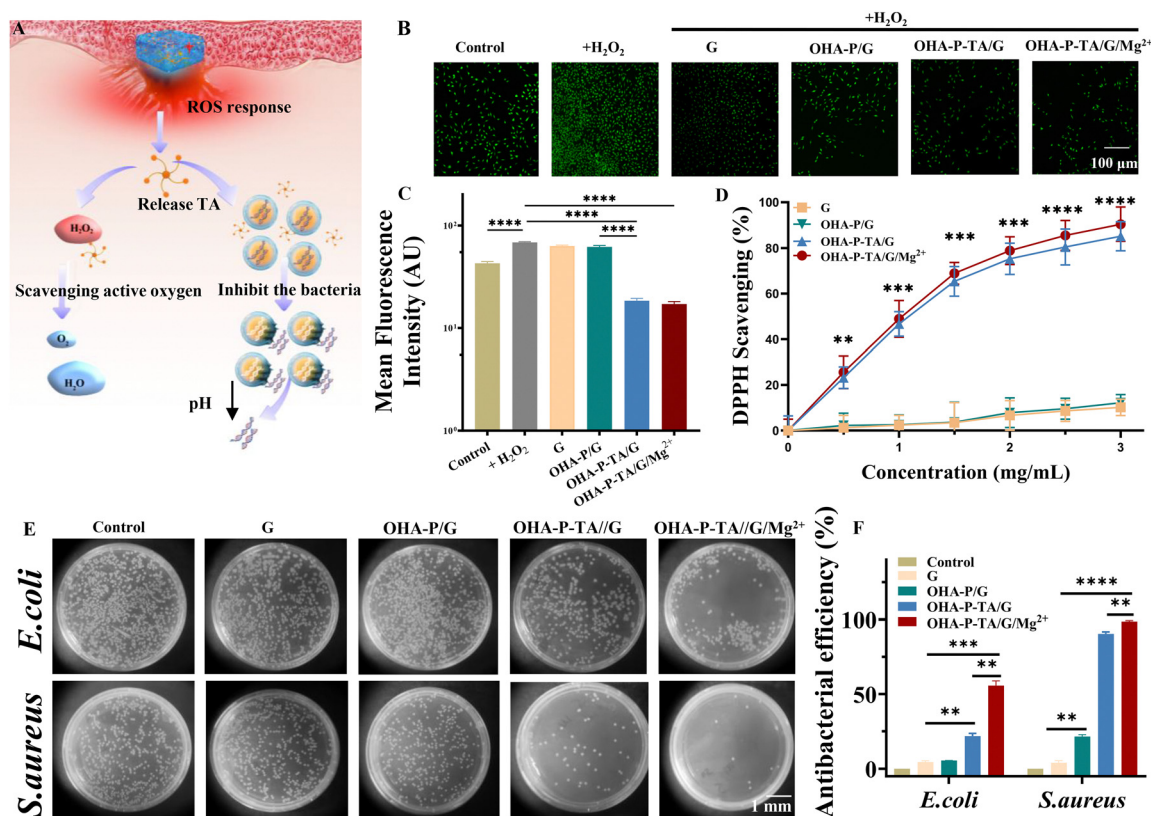


Fig. 3 Antioxidant and bactericidal ability of hydrogels. (A) The mechanism diagram of the hydrogel. (B) *In vitro* reactive oxygen species scavenging assay. (C) Mean fluorescence intensity quantified by the active oxygen probe. (D) DPPH scavenging rate by different components of the hydrogels. (E) The viable colony units (*E. coli* and *S. aureus*) grew on the plates incubated with hydrogel extracts. (F) Antibacterial effects of *E. coli* and *S. aureus* cultured by different components of the hydrogels. Data are shown as mean \pm SD, $n = 3$. * $p < 0.05$, ** $p < 0.01$, *** $p < 0.001$, **** $p < 0.0001$.

(Fig. S6A and B, ESI[†]). These findings indicated that OHA-P-TA/G/Mg²⁺ hydrogels have the ability to effectively neutralize ROS generated within cells, thus safeguarding cells from the damaging effects of oxidative stress during the wound healing process.

Antibacterial activity is a crucial property of wound dressings, given that wounds that are open and exuding are susceptible to colonization and multiplication by a variety of bacteria. *S. aureus* and *E. coli* are frequently encountered pathogens in wounds with chronic infections. As depicted in Fig. 3(E) and (F), the OHA-P-TA/G and OHA-P-TA/G/Mg²⁺ hydrogels had the fewest colonies, particularly in *S. aureus*, suggesting that these two groups exhibited the most potent antibacterial effectiveness. Remarkably, almost all *S. aureus* were eliminated following contact with the OHA-P-TA/G/Mg²⁺ hydrogel. The OHA-P-TA/G and OHA-P-TA/G/Mg²⁺ hydrogels showed the antibacterial rates of 89.90 ± 1.30% and 92.20 ± 0.42% for *S. aureus*, and 23.40 ± 0.68% and 53.85 ± 0.38% for *E. coli*, respectively (Fig. 3(F)). The bacteriostatic effect of the hydrogel against *S. aureus* was further evaluated using the bacteriostatic ring assay. Compared to the G hydrogel, the OHA-P-TA/G and OHA-P-TA/G/Mg²⁺ hydrogels demonstrated an antibacterial effect for up to 24 h. After 24 h, OHA-P-TA/G and OHA-P-TA/G/Mg²⁺ produced larger inhibition circles of 8.57 ± 0.50 and 10.86 ± 0.51 mm, respectively, against *S. aureus*. The zone of inhibition (ZOI) of the OHA-P-TA/G/Mg²⁺ hydrogel was larger than that of the OHA-P-TA/G hydrogel, presumably because the halo size was related to TA release and Mg²⁺ (Fig. S6C and D, ESI[†]). These findings indicate that the antibacterial efficacy of the OHA-P-TA/G/Mg²⁺ hydrogels is likely to be more potent against *S. aureus* compared to *E. coli*. This could be attributed to the varying capabilities of TA to infiltrate bacterial cell membranes or the differing affinities of the respective bacterial receptors. Collectively, these results verified that the OHA-P-TA/G/Mg²⁺ hydrogel gradually initiates a response that programmatically releases TA, initiating an acute inflammatory phase that achieves scavenging of reactive oxygen species and disruption of bacterial cell membranes, with magnesium ions acting synergistically throughout the process in high ROS and infected bacterial wounds.¹⁴

3.5 Effects on cell proliferation, migration, and angiogenesis *in vitro*

The cytocompatibility of hydrogels was evaluated using live/dead staining and CCK-8 assay. All prepared hydrogel extracts were separately incubated with L929 cells for 1, 3, and 5 days. FDA/PI staining results showed an increase in the number of live cells over time across all groups (Fig. 4(A)). As shown in Fig. 4(B), there was no significant difference in cell viability among the hydrogel groups compared to the control on day 1. However, cell viability in the OHA-P-TA/G and OHA-P-TA/G/Mg²⁺ hydrogels significantly increased on days 3 and 5 ($p < 0.05$). In contrast, the cell proliferation rate in the OHA-P/G was slower than in the OHA-P-TA/G, although the OHA-P-TA/G/Mg²⁺ still demonstrated significant potential for promoting cell proliferation ($p < 0.05$). Furthermore, a cell scratch model

was used to evaluate the *in vitro* cell migration effect of the hydrogels, and the migration of co-cultured L929 cells was further assessed. Hydrogel groups containing TA significantly enhanced cell migration compared to the control group in the H₂O₂-induced model (Fig. 4(C)). After 24 h, the cell scratch healing rates for the control, G, OHA-P/G, OHA-P-TA/G, and OHA-P-TA/G/Mg²⁺ were 19.98 ± 0.76%, 23.23 ± 2.82%, 47.05 ± 2.82%, and 67.67 ± 4.37%, respectively (Fig. 4(D)). These findings imply that the OHA-P-TA/G and OHA-P-TA/G/Mg²⁺ hydrogels demonstrated superior cytocompatibility and fostered *in vitro* cell growth and movement, which could be advantageous for the restoration of injured tissues. The regeneration of blood vessels is a key factor in the healing of skin wounds and the regeneration of tissues. To investigate the capacity of the hydrogels to stimulate angiogenesis, tube formation experiments were conducted *in vitro* using human umbilical vein endothelial cells (HUVECs).²⁶ In contrast to the control group, the vascular-like structures formed by the OHA-P-TA/G and OHA-P-TA/G/Mg²⁺ hydrogel groups were denser after 10 h (Fig. 4(E)). HUVECs cultured with the OHA-P-TA/G/Mg²⁺ hydrogel extract showed more total branching length than the control, G, OHA-P/G, and OHA-P-TA/G (Fig. 4(F)). These findings could be credited to Mg²⁺, validating the capacity of the OHA-P-TA/G/Mg²⁺ hydrogels to stimulate angiogenesis. Additionally, the blood compatibility of the hydrogel was assessed through a hemolysis assay, given that the hemolytic rate (HR) is deemed a crucial measure for evaluating the compatibility of biomaterials. A dressing, which adheres to the wound during treatment, is expected to demonstrate a high degree of hemocompatibility from a biocompatibility standpoint. Hence, a hemolysis test was selected to gauge the hemocompatibility of the hydrogel. The data in Fig. S7A and B (ESI[†]) show a hemolysis ratio of less than 5% for all hydrogel groups, indicating good hemocompatibility of the hydrogels.

3.6 Elevated anti-inflammatory effects and macrophage polarization modulation *in vitro*

The initiation of remodeling in infected wounds is determined by the successful transition through the acute inflammatory phase. Macrophages, known for triggering both localized and systemic defense reactions and releasing inflammatory cytokines, are instrumental during the inflammation stage of wound recovery (Fig. 5(A)).^{26,27} In this study, the anti-inflammatory potential of the hydrogels was assessed using RAW 264.7 macrophages. These macrophages were initially induced with LPS and then exposed to different hydrogel extracts over a period of 24 h. As shown in Fig. S8 (ESI[†]), the cell viability in the OHA-P-TA/G and OHA-P-TA/G/Mg²⁺ hydrogel groups significantly increased at 1 and 2 days, according to the CCK-8 method. This increase was primarily attributed to the hydrogel's ability to inhibit macrophage inflammation. Nitric oxide (NO), a key cytokine that mediates the inflammatory response, plays a significant role in endotoxin-induced organismal injury. It can significantly augment the secretion of NO in LPS-stimulated RAW 264.7 cells. The Raw264.7 cells treated with all hydrogel extracts were collected for flow cytometry

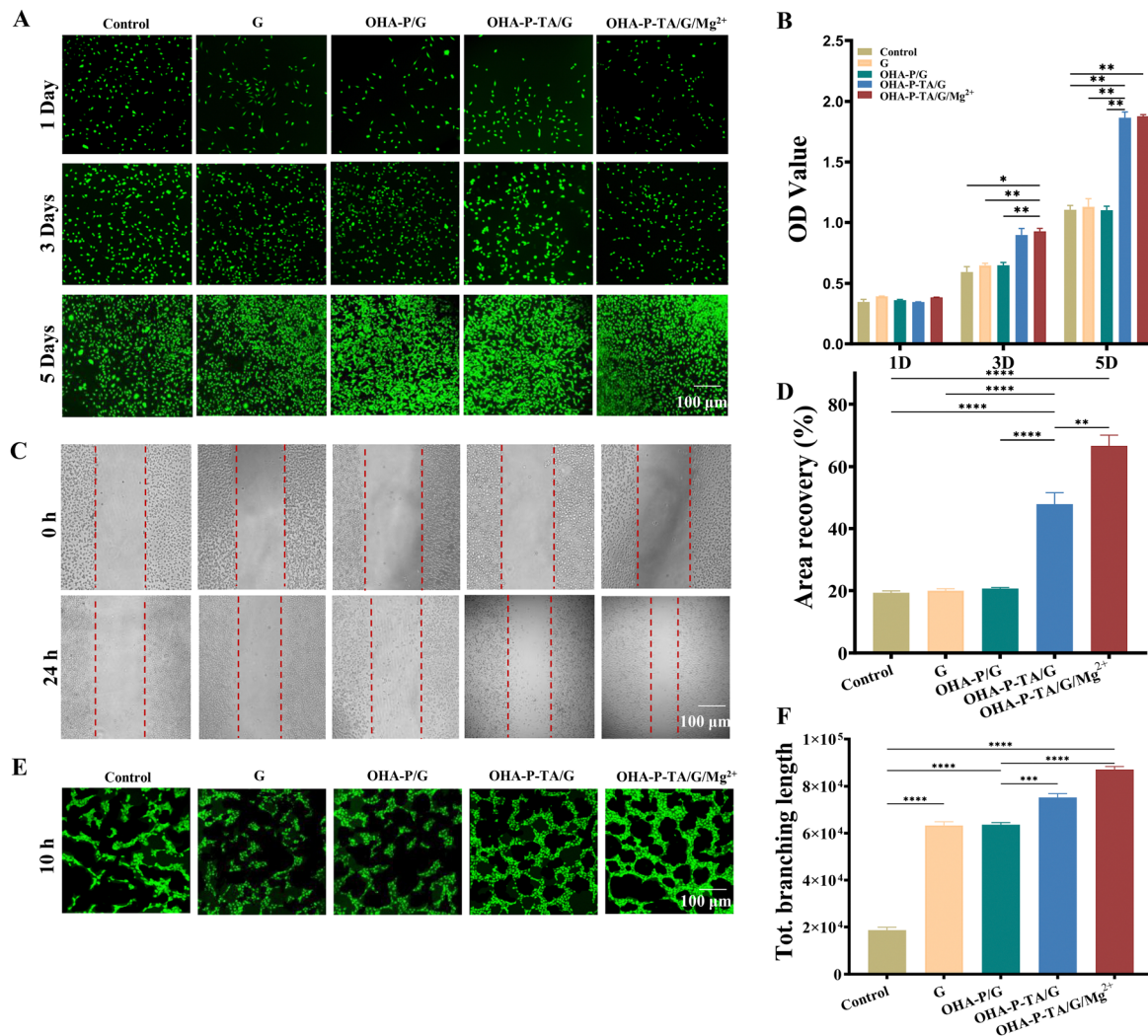


Fig. 4 *In vitro* biocompatibility evaluation of hydrogels. (A) Representative images of FDA/PI staining for L929 cells from each group after 1 day, 3 days and 5 days (scale bar: 100 μ m). (B) The proliferation of L929 cells quantified using the CCK-8 kit. (C) The migration images of L929 cells in a serum-free medium, captured at 0 and 24 h (scale bar: 100 μ m). (D) Statistics related to the area recovery of L929 cells. (E) Illustrations of HUVEC angiogenesis under various treatments (scale bar: 100 μ m). (F) The cumulative branching length from the *in vitro* tube formation experiments. Data are shown as mean \pm SD, $n = 3$. * $p < 0.05$, ** $p < 0.01$, *** $p < 0.001$, **** $p < 0.0001$.

analysis using DAF-FM DA. The data from the hydrogel extracts containing TA showed a decrease in fluorescence intensity compared to the group treated with LPS alone (Fig. 5(B)). The NO test kit results revealed that the OHA-P-TA/G/Mg²⁺ solution and the OHA-P-TA/G extract reduced NO production to 70.77% and 40.24% respectively, compared to the group treated with the LPS stimulated alone group (Fig. 5(C)). These results confirmed the superior ability of OHA-P-TA/G/Mg²⁺ in reducing NO levels.

In a chronic wound, the accumulation of M1 macrophages and the impaired transition of M2 macrophages can intensify tissue injury and hinder wound healing. A notable feature of macrophages during M2 polarization is the heightened expression of the surface marker CD206, whereas M1 macrophages are distinguished by the surface marker CD86 or intracellular iNOS. We employed flow cytometry analysis and

immunofluorescence staining to ascertain the impact of the hydrogels on macrophage polarization. As depicted in Fig. 5(D) and (E), there was a noticeable increase in the proportion of M1 macrophages (CD86+) following the addition of LPS. In contrast, after intervention with the OHA-P-TA/G/Mg²⁺ hydrogel, a significant decrease in the proportion of M1 macrophages (CD86+) and an increase in the proportion of M2 macrophages (CD206+) were observed. There were no significant changes in M2 macrophages (CD206+) after treatment with the OHA-P-TA/G, suggesting that Mg²⁺ is essential for the process of OHA-P-TA/G hydrogel polarization. However, the OHA-P/G/Mg²⁺ hydrogel had no effect on promoting M2 macrophages (CD206+). This indicates that the roles of TA and Mg²⁺ in immune regulation are complementary, and can only be achieved by ensuring the smooth transition of various stages. The OHA-P/G hydrogel, which contained either TA or Mg²⁺, could not initiate

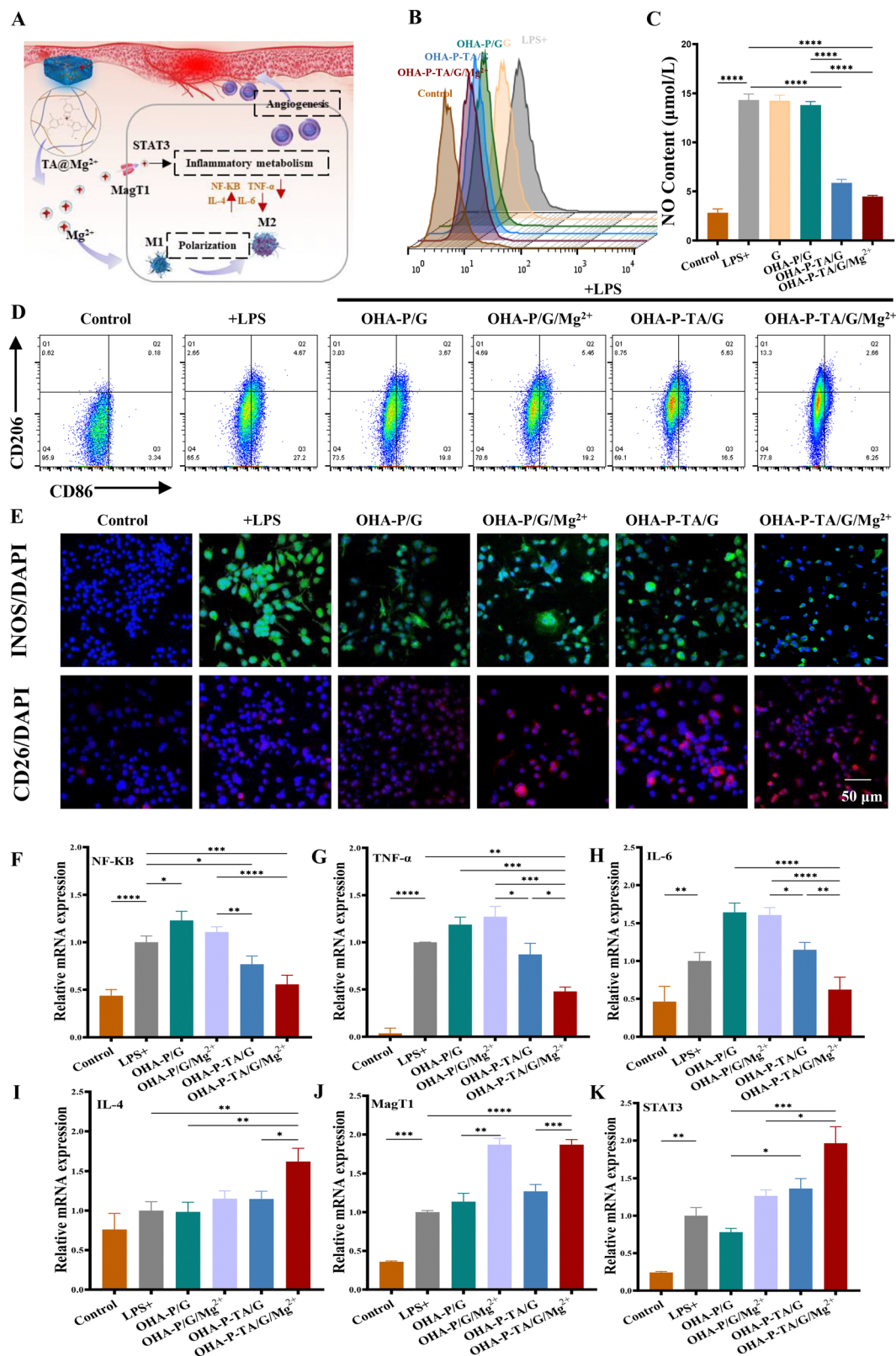


Fig. 5 The anti-inflammatory effects of the hydrogels. (A) Schematic illustration of the immunoregulatory activity of the OHA-P-TA/G/Mg²⁺ hydrogel. (B) Flow analysis of NO fluorescence staining after different treatments. (C) Measurement of the NO content. (D) The expression of M1 (CD86+) and M2 (CD206+) in different groups detected by flow cytometry. (E) Immunofluorescence staining images of M1 (INOS) and M2 (CD206+) macrophages. (F)–(I) The relative mRNA of NF-κB, TNF-α, IL-6 and IL-4 of macrophages. (J) and (K) The relative mRNA of MagT1 and STAT3 of macrophages. Data are shown as mean ± SD, *n* = 3. **p* < 0.05, ***p* < 0.01, ****p* < 0.001, *****p* < 0.0001.

the process of promoting macrophage polarization to M2. The OHA-P-TA/G/Mg²⁺ hydrogel achieved anti-inflammatory effects by first reducing the conversion of macrophages to M1 with TA, and then further promoting the process of macrophage polarization to M2 with Mg²⁺.

In order to further confirm the state of macrophage polarization and anti-inflammatory activity, RT-qPCR is utilized to detect the gene expression of specific markers. NF-κB, which plays a key role in the regulation of cytokine-induced gene expression and is involved in many biological processes such as immune response, inflammatory response, and apoptosis, shows a remarkable decrease in gene expression in the OHA-P-TA/G and OHA-P-TA/G/Mg²⁺ hydrogel groups (Fig. 5(F)). The gene expression of M1 markers (TNF-α and IL-6) shows remarkably decreased levels in the OHA-P-TA/G and OHA-P-TA/G/Mg²⁺ hydrogel groups (Fig. 5(G) and (H)), demonstrating a decline of M1 phenotype. Conversely, the gene expression of IL-4 is significantly upregulated only in the OHA-P-TA/G/Mg²⁺ hydrogel group compared to the group with LPS (*p* < 0.0001), suggesting enhanced M2 activity (Fig. 5(I)). Meanwhile, we found that the gene expression of MagT1 was up-regulated by OHA-P/G/Mg²⁺ and OHA-P-TA/G/Mg²⁺ compared to the group treated with LPS (Fig. 5(J)). However, the gene expression of STAT3 was significantly up-regulated by the OHA-P-TA/G/Mg²⁺ hydrogel compared to the group only with LPS (Fig. 5(K)). These results suggest that the OHA-P-TA/G/Mg²⁺ hydrogel induced M2 macrophage polarization, thereby confirming our hypothesis. TA@Mg²⁺ can synergistically activate magnesium ion channels (MagT1) and influence the phosphorylation level of STAT3 proteins, which mediate the proliferation, migration and anti-inflammation through the p-STAT3 pathway.^{28,29}

3.7 Acceleration of wound healing with antibacterial effects *in vivo*

An optimal hydrogel dressing was identified to combine excellent biocompatibility, promotion of wound healing, and resistance to infections. Based on *in vitro* findings, OHA-P/G, OHA-P-TA/G, and OHA-P-TA/G/Mg²⁺ were selected for *in vivo* experiments. The hydrogel was injected into the entire *S. aureus*-infected wound *in situ* (Fig. 6(A)) and compared with a control group treated with a commercial Tegaderm film. The dressings made of hydrogel were replaced at 3-day intervals. Fig. 6(B) presents illustrative images of wounds from different groups at predetermined time points. Macroscopically, the OHA-P-TA/G/Mg²⁺ hydrogel demonstrated significantly superior efficacy in wound healing compared to the other groups, with the OHA-P-TA/G/Mg²⁺ group showing no noticeable wounds after 12 days of treatment. In addition, the areas of the wounds and the progress of wound closure were quantified based on the photograph of the wounds (refer to Fig. 6(C)). After a treatment period of three days, the Control, OHA-P/G, OHA-P-TA/G, and OHA-P-TA/G/Mg²⁺ hydrogel groups exhibited wound closures of 14.86%, 15.10%, 23.19%, and 34.01%, respectively. By the 8th day, the wound closure in the OHA-P-TA/G/Mg²⁺ hydrogel group was 73.30%, which was significantly greater than that of the other groups.

The antibacterial capabilities of the synthesized hydrogels were assessed *in vivo* by collecting and quantifying bacteria from the wound site using the spread plate technique after a treatment period of 2 days. As depicted in Fig. 6(E) and (F), a minimal number of viable colonies were observed on the TSA post 2-day treatment with OHA-P-TA/G and OHA-P-TA/G/Mg²⁺. Conversely, the wound tissues from the control and OHA-P/G groups displayed robust bacterial activity with a substantial formation of colonies. This evidence suggests that the OHA-P-TA/G/Mg²⁺ hydrogel effectively eradicates bacteria *in vivo*. In this investigation, all hydrogel groups demonstrated superior wound healing rates compared to the control group treated with the Tegaderm film, possibly due to the film's restricted biological functionality. Moreover, the OHA-P-TA/G/Mg²⁺ hydrogel group exhibited significantly enhanced wound healing compared to the OHA-P-TA/G and OHA-P/G groups. These findings unequivocally suggest that the TA@Mg²⁺ driven hydrogel modifies the wound infection milieu, fostering a sterile and conducive environment to expedite the healing of infected wounds.

3.8 Improved quality of regenerated skin dermis's ECM *in vivo*

In order to delve deeper into the impact of the hydrogel on wound recovery, the healing process was monitored using Hematoxylin and Eosin (H&E) staining. The group treated with the Tegaderm film exhibited a significant presence of inflammatory cells on the 6th day, a severe condition that continued until the 12th day (Fig. 7(A)). Despite the emergence of new epidermal tissue in the wound treated with the OHA-P-TA/G hydrogel, the persistent inflammation hindered the successful repair of the infected wound. On the other hand, the OHA-P-TA/G/Mg²⁺ group demonstrated an increase in hair follicles, a decrease in neutrophils, and the most rapid wound healing process. The epidermal thickness and hair follicle formation were quantified on day 6 and on day 12, and the OHA-P-TA/G/Mg²⁺ group outperformed other groups significantly (Fig. 7(C) and (D)). Masson's trichrome staining can be used to react to the deposition and arrangement of collagen during the healing process of infected wounds. The wounds treated with the hydrogel demonstrated a more concentrated and darker blue collagen accumulation, contrasting sharply with the control wounds where collagen accumulation was scant and light during the healing process (Fig. 7(B)). As depicted in Fig. 7(B) and (E), an increase in collagen accumulation in the wound area was observed in the OHA-P-TA/G/Mg²⁺ groups on day 6. The collagen fibers of the control and OHA-P/G groups remained partially disorganized. However, by day 12, the collagen depositions in the OHA-P-TA/G and OHA-P-TA/G/Mg²⁺ groups were denser and more organized, reflecting the morphology, structural integrity, and appendages of normal skin tissues (Fig. 7(E)). These findings underscore the potential of the OHA-P-TA/G/Mg²⁺ hydrogel dressing to significantly expedite tissue regeneration and the wound healing process.

The ECM of the skin dermis, primarily composed of Col I (yellow or red) and Col III (green), was distinguishable using

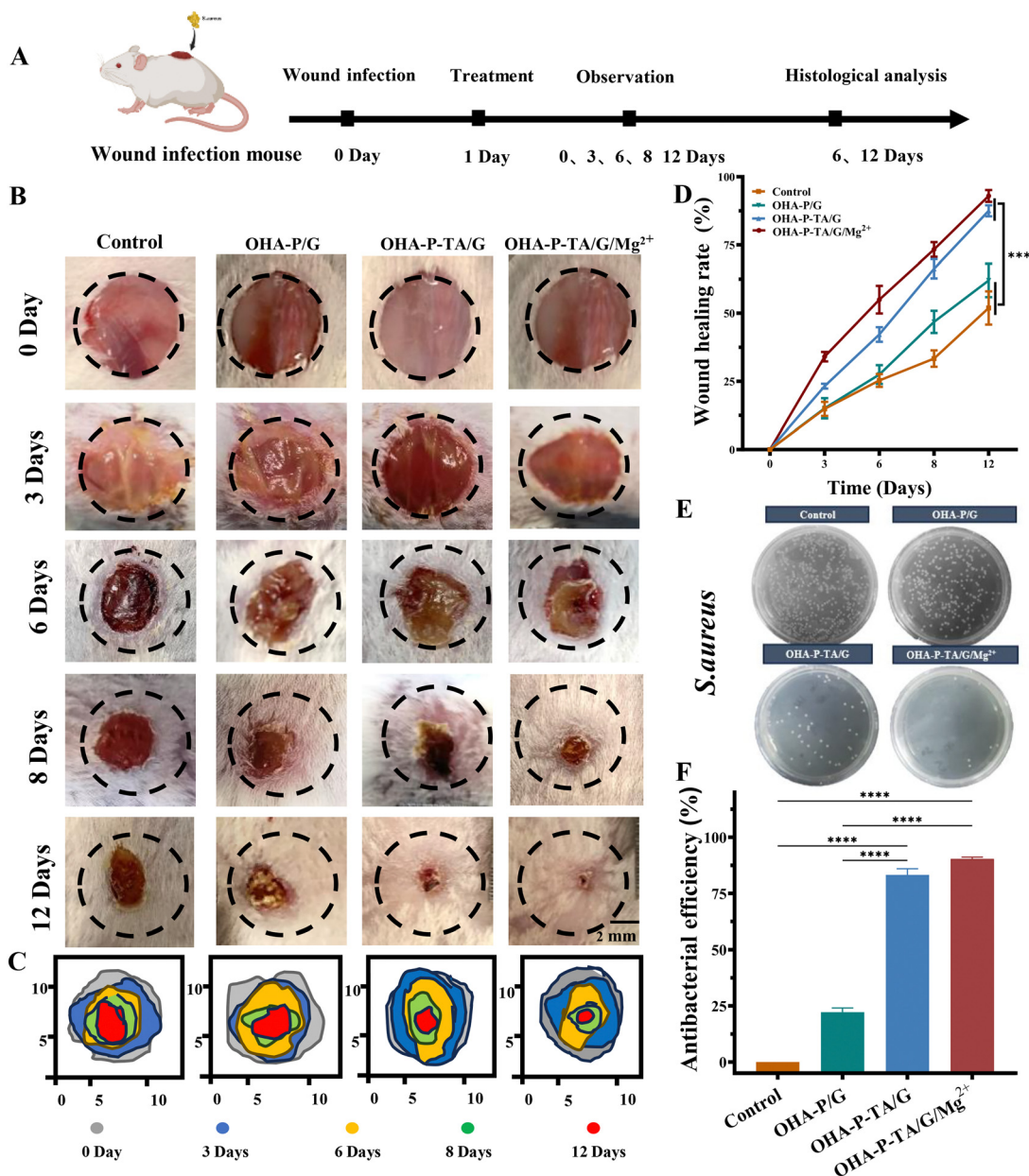


Fig. 6 Infected wound healing experiments *in vivo*. (A) The process of healing across the entire wound layer in the presence of an *in vivo* *S. aureus* infection. (B) Macroscopic photograph of the wounds subjected to various treatments, captured on different days for each group. (C) Progression of wound healing over a span of 12 days following treatment with different hydrogels. (D) Wound contraction rate within the 12 days. (E) Images showcasing the presence of live bacteria on the TSA after 2 days of undergoing different treatments *in vivo*. (F) The antibacterial rate of different hydrogels in combating *S. aureus*, as determined by the spread plate method. Data are shown as mean \pm SD, $n = 6$. * $p < 0.05$, ** $p < 0.01$, *** $p < 0.001$, **** $p < 0.0001$.

Sirius Red staining and polarizing microscopy.¹⁷ The distribution of both yellow and green colors in the control group was noticeably sparser than that in the OHA-P-TA/G and OHA-P-TA/G/Mg²⁺ groups, indicating damage to the dermis and a decrease in Col I and Col III. Fig. 7(F) shows that both Col I and Col III in the dermis increased and distributed evenly in the OHA-P-TA/G/Mg²⁺ hydrogel as the healing process advanced, and the collagen structure became more similar to the network structure of normal skin. The proportion of Col I and Col III increased over time, while the proportion of type III collagen

in the OHA-P-TA/G/Mg²⁺ group increased more significantly, indicating collagen secretion and accumulation influenced by TA and Mg²⁺. On day 12, the proportions of Col III in the control group, OHA-P/G, OHA-P-TA/G, OHA-P-TA/G/Mg²⁺ hydrogels were $1.09 \pm 0.14\%$, $1.27 \pm 0.15\%$, $1.53 \pm 0.19\%$, $1.92 \pm 0.15\%$ and $2.63 \pm 0.42\%$, respectively (Fig. 7(G) and (H)). Collectively, the data suggested that the OHA-P-TA/G/Mg²⁺ hydrogel significantly promoted collagen deposition at the infected wound site, thereby accelerating the closure and regeneration of the skin wound. Moreover, gross observations

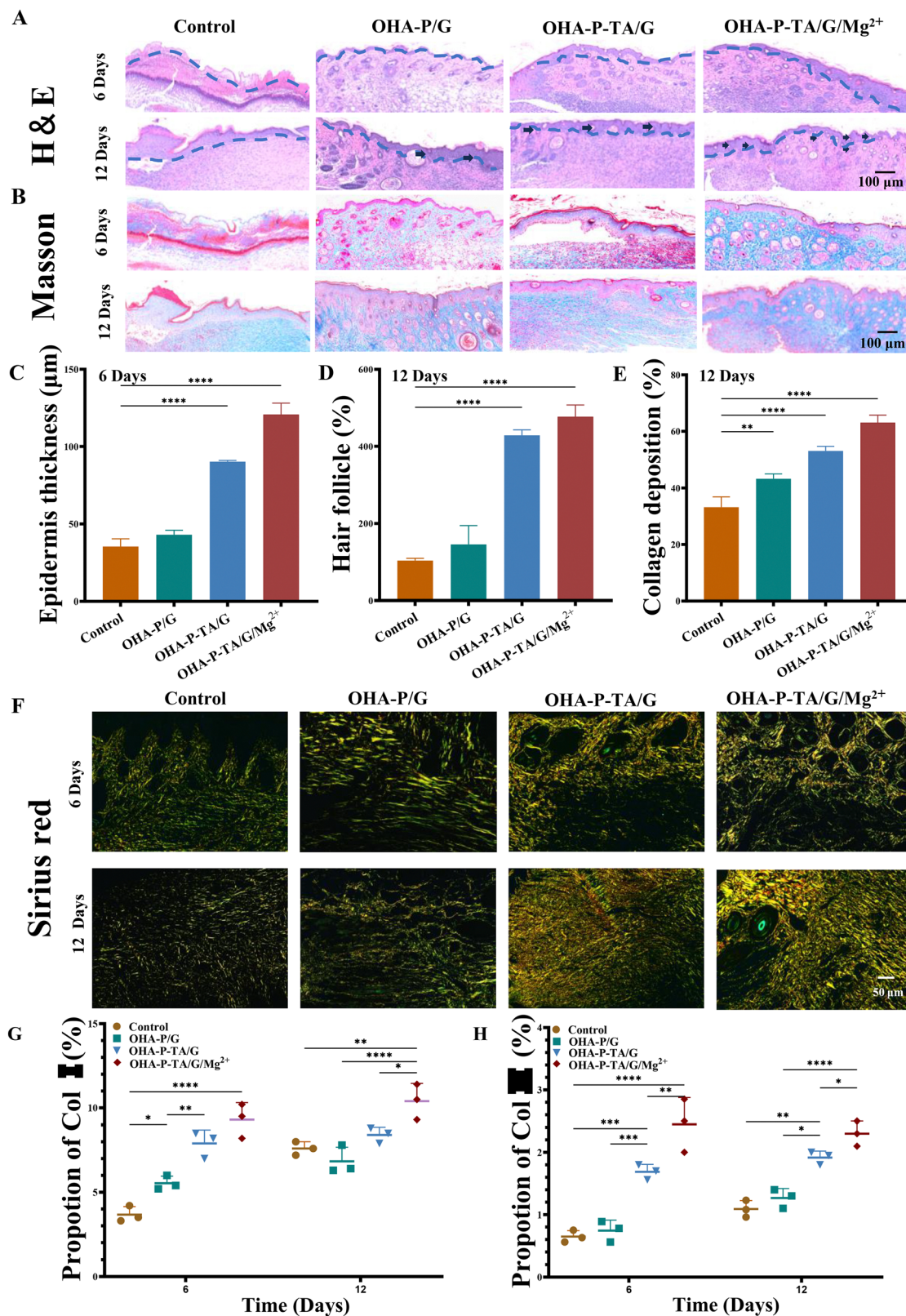


Fig. 7 Histological analysis of wound across various groups. (A) and (B) Sections of wound tissue treated with different samples, stained with H&E and Masson's trichrome on day 6 and 12 (arrow: hair follicle). (C) Measurement of the thickness of the epidermis in each group on day 6. (D) Count of hair follicles in each group on day 12. (E) Assessment of collagen deposition in each group on day 12. (F) Images of Sirius Red staining on days 6 and 12, showcasing the newly regenerated skin tissues for each group. (G) The ratio of Col I. (H) The ratio of Col III. Data are shown as mean \pm SD, $n = 6$. * $p < 0.05$, ** $p < 0.01$, *** $p < 0.001$, and **** $p < 0.0001$.

and pathologic sections showed no damage to major organs (heart, liver, spleen, lungs, and kidneys) after 12 days (Fig. S9, ESI[†]), which again proved that the hydrogels did not cause significant local or systemic toxicity in mice during the degradation process.

3.9 Anti-inflammatory and vascularization effects *in vivo*

Persistent inflammation is a key characteristic of chronic wounds, and a shift from an inflammatory state to a proliferative one is recognized as a vital control point in wound healing.^{1,29} After 12 days of treatment, immunohistochemistry staining images revealed an increase in the expression of TNF- α and IL-6 in the control group and the OHA-P/G hydrogel group, and a decrease in expression in the OHA-P-TA/G and OHA-P-TA/G/Mg²⁺ groups (Fig. 8(A) and Fig. S10A, B, ESI[†]). The IL-4 expression noticeably increased in the OHA-P-TA/G/Mg²⁺ group

compared to other groups (Fig. 8(A) and Fig. S10C, ESI[†]). In addition, the expressions of Ki67 (a nuclear protein linked to cellular proliferation) and VEGF (which promotes blood vessel growth for wound recovery) were selected to evaluate the regeneration process of wound healing.³⁰ The OHA-P-TA/G/Mg²⁺ hydrogel further promoted Ki67 and VEGF expression on day 12 compared to other groups (Fig. 8(A) and Fig. S10D, E, ESI[†]), corroborating the ELISA results (Fig. 8(B)–(E)). These findings suggested that the OHA-P-TA/G/Mg²⁺ hydrogel effectively reduced the expression of pro-inflammatory factors and increased the expression of anti-inflammatory factors to initiate an immune response, thus promoting cell proliferation and remodeling vascularization to achieve regeneration of skin tissue. Although a multifunctional hydrogel has been developed for treating infected skin injuries, current research still faces certain limitations. Firstly, the optimal loading amounts

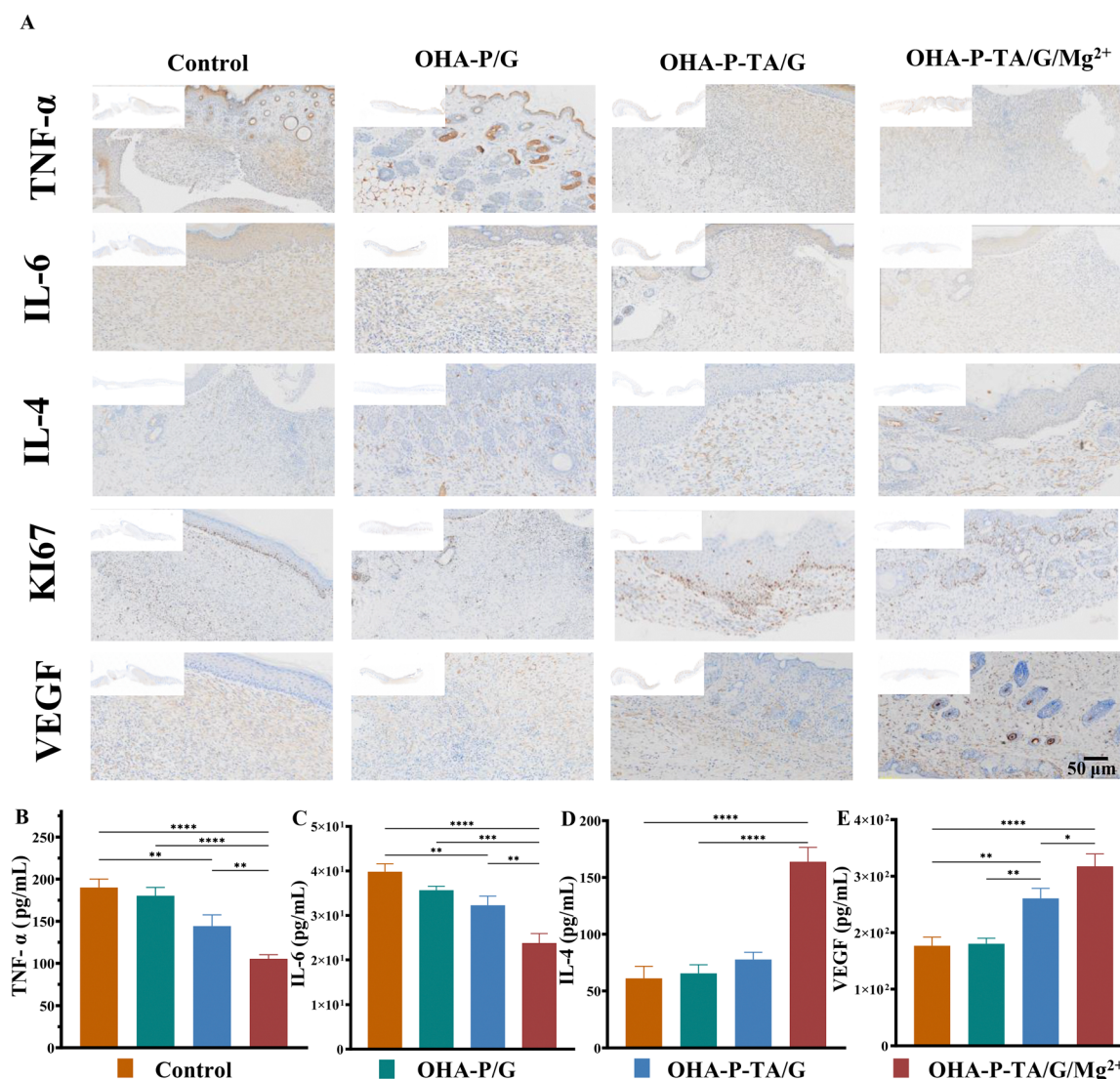


Fig. 8 *In vivo* immunoregulatory, anti-inflammatory, and neovascularization activities of the hydrogels. (A) Immunohistochemistry staining images of TNF- α , IL-6, IL-4, Ki67 and VEGF of the regenerated skin in different groups on day 12 (scar bar: 50 μ m). (B)–(E) The expression of TNF- α , IL-6, IL-4 and VEGF in the regenerated skin in different groups was detected by ELISA on day 6. Data are shown as mean \pm SD, $n = 6$. * $p < 0.05$, ** $p < 0.01$, *** $p < 0.001$, and **** $p < 0.0001$.

of TA and Mg^{2+} need to be further refined. The incorporation of TA and Mg^{2+} into the hydrogel confers antioxidation, anti-inflammatory, and pro-angiogenic properties. Consequently, it is anticipated that future research will identify an optimized combination that maximizes these functional benefits. Secondly, the synergistic mechanism of TA and Mg^{2+} in treating infected wounds requires further investigation in the subsequent research.

4. Conclusions

This study focuses on the development of an injectable hydrogel with self-healing, antibacterial, antioxidant, and anti-inflammatory properties for treating chronic infected wounds. The hydrogels, crafted from OHA-P-TA and G polymers, possess robust mechanical durability, self-repairing capabilities, and are responsive to pH/ROS stimuli, attributes that are attributed to the structure of a dynamic Schiff base and boronic ester bonds. This multifunctional hydrogel can effectively eliminate surplus free radicals and curb the production of ROS, thereby mitigating oxidative stress damage and providing antibacterial effects through the spatiotemporal release of TA. Furthermore, the TA@ Mg^{2+} driven hydrogel alters the wound infection conditions, fostering a clean and conducive environment that expedites the healing process of infected wounds. TA promptly controls the acute inflammatory phase, while Mg^{2+} enables chronic wounds to transition swiftly to the next phase. *In vivo* animal tests show that the OHA-P-TA/G/ Mg^{2+} hydrogel can improve epithelial regeneration, collagen deposition, and neovascularization, thereby accelerating wound healing. Collectively, the OHA-P-TA/G/ Mg^{2+} hydrogel demonstrates promising potential as a wound dressing for promoting infected wound repair.

Author contributions

Na Li: conceptualization, investigation, writing – original draft, and formal analysis. Yi Cao: software and investigation. Jingyi Liu: software and investigation. Wen Zou: investigation. Manyu Chen: investigation. Hongfu Cao: investigation. Siyan Deng: investigation. Chen Zhou: investigation. Jie Liang: validation and resources. Tun Yun: validation. Xingdong Zhang: funding acquisition, project administration, and writing – review & editing. Yujiang Fan: funding acquisition, project administration, and writing – review & editing. Qiguang Wang: funding acquisition, project administration, and writing – review & editing.

Data availability

The data supporting this article have been included as part of the ESI.†

Conflicts of interest

The authors declare that they have no known competing financial interests or personal relationships that could have appeared to influence the work reported in this paper.

Acknowledgements

This work was supported by the National Key R&D Project of China (no. 2022YFC2401800) and the 111 Project (B16033).

References

- 1 Y. Yang, C. Chu, L. Liu, C. Wang, C. Hu, S. Rung, Y. Man and Y. Qu, Tracing immune cells around biomaterials with spatial anchors during large-scale wound regeneration, *Nat. Commun.*, 2023, **14**, 5995.
- 2 G. C. Gurtner, S. Werner, Y. Barrandon and M. T. Longaker, Wound repair and regeneration, *Nature*, 2008, **453**, 314–321.
- 3 J. Xu, C. Yu, S. Wang, L. Xiong, F. Geng, J. Lv, L. Zhao and Y. Wang, Quantitative generation of ROS and their effective photocatalytic antibacterial activity of high-intensity universal P25 network films: The role of ROS, *J. Environ. Chem. Eng.*, 2023, **11**, 110915.
- 4 P. Bhattacharya, A. Dey and S. Neogi, An insight into the mechanism of antibacterial activity by magnesium oxide nanoparticles, *J. Mater. Chem. B*, 2021, **9**, 5329–5339.
- 5 Z. Ghilissi, R. Kallel, A. Sila, B. Harrabi, R. Atheymen, K. Zeghal, A. Bougatef and Z. Sahnoun, Globularia alypum methanolic extract improves burn wound healing process and inflammation in rats and possesses antibacterial and antioxidant activities, *Biomed. Pharmacother.*, 2016, **84**, 1488–1495.
- 6 S. B. Doernberg, L. Komarow, T. T. T. Tran, Z. Sund, M. W. Pandori, D. Jensen, E. L. Tsalik, C. D. Deal, H. F. Chambers, V. G. Fowler, Jr., S. R. Evans, R. Patel and J. D. Klausner, Simultaneous Evaluation of Diagnostic Assays for Pharyngeal and Rectal Neisseria gonorrhoeae and Chlamydia trachomatis Using a Master Protocol, *Clin. Infect. Dis.*, 2020, **71**, 2314–2322.
- 7 J. Mao, J.-H. Kim and S. Seo, Current Status and Outlook of Low-Melting-Point Metals in Biomedical Applications, *Adv. Funct. Mater.*, 2023, 2307708.
- 8 D. Bi, F. Qu, W. Xiao, J. Wu, P. Liu, H. Du, Y. Xie, H. Liu, L. Zhang, J. Tao, Y. Liu and J. Zhu, Reactive Oxygen Species-Responsive Gel-Based Microneedle Patches for Prolonged and Intelligent Psoriasis Management, *ACS Nano*, 2023, **17**, 4346–4357.
- 9 R. Vijayaraghavan, S. Loganathan and R. B. Valapa, 3D bioprinted photo crosslinkable GelMA/methylcellulose hydrogel mimicking native corneal model with enhanced in vitro cytocompatibility and sustained keratocyte phenotype for stromal regeneration, *Int. J. Biol. Macromol.*, 2024, **264**, 130472.
- 10 L.-M. Zhang, C.-X. Wu, J.-Y. Huang, X.-H. Peng, P. Chen and S.-Q. Tang, Synthesis and characterization of a degradable

- composite agarose/HA hydrogel, *Carbohydr. Polym.*, 2012, **88**, 1445–1452.
- 11 S. Y. Wang, H. Kim, G. Kwak, H. Y. Yoon, S. D. Jo, J. E. Lee, D. Cho, I. C. Kwon and S. H. Kim, Development of Biocompatible HA Hydrogels Embedded with a New Synthetic Peptide Promoting Cellular Migration for Advanced Wound Care Management, *Adv. Sci.*, 2018, **5**, 1800852.
 - 12 Y. Yang, X. Zhao, J. Yu, X. Chen, R. Wang, M. Zhang, Q. Zhang, Y. Zhang, S. Wang and Y. Cheng, Bioactive skin-mimicking hydrogel band-aids for diabetic wound healing and infectious skin incision treatment, *Bioact. Mater.*, 2021, **6**, 3962–3975.
 - 13 N. Xu, Y. Gao, Z. Li, Y. Chen, M. Liu, J. Jia, R. Zeng, G. Luo, J. Li and Y. Yu, Immunoregulatory hydrogel decorated with Tannic acid/Ferric ion accelerates diabetic wound healing via regulating Macrophage polarization, *Chem. Eng. J.*, 2023, **466**, 143173.
 - 14 M. Li, X. Shi, B. Yang, J. Qin, X. Han, W. Peng, Y. He, H. Mao, D. Kong and Z. Gu, Single-component hyaluronic acid hydrogel adhesive based on phenylboronic ester bonds for hemostasis and wound closure, *Carbohydr. Polym.*, 2022, **296**, 119953.
 - 15 W. Chen, C. Wang, W. Liu, B. Zhao, Z. Zeng, F. Long, C. Wang, S. Li, N. Lin and J. Zhou, A Matrix-Metalloproteinase-Responsive Hydrogel System for Modulating the Immune Microenvironment in Myocardial Infarction, *Adv. Mater.*, 2023, **35**, 2209041.
 - 16 Z. Guo, Z. Zhang, N. Zhang, W. Gao, J. Li, Y. Pu, B. He and J. Xie, Mg⁽²⁺⁾/polydopamine composite hydrogel for the acceleration of infected wound healing, *Bioact. Mater.*, 2022, **15**, 203–213.
 - 17 H. Ren, Z. Zhang, X. Cheng, Z. Zou, X. Chen and C. He, Injectable, self-healing hydrogel adhesives with firm tissue adhesion and on-demand biodegradation for sutureless wound closure, *Sci. Adv.*, 2023, **9**, eadh4327.
 - 18 J. Jing, S. Liang, Y. Yan, X. Tian and X. Li, Fabrication of Hybrid Hydrogels from Silk Fibroin and Tannic Acid with Enhanced Gelation and Antibacterial Activities, *ACS Biomater. Sci. Eng.*, 2019, **5**, 4601–4611.
 - 19 J. Pan, H. Liao, G. Gong, Y. He, Q. Wang, L. Qin, Y. Zhang, H. Ejima, B. L. Tardy, J. J. Richardson, J. Shang, O. J. Rojas, Y. Zeng and J. Guo, Supramolecular nanoarchitectonics of phenolic-based nanofiller for controlled diffusion of versatile drugs in hydrogels, *J. Controlled Release*, 2023, **360**, 433–446.
 - 20 X. Zhao, Y. Yang, J. Yu, R. Ding, D. Pei, Y. Zhang, G. He, Y. Cheng and A. Li, Injectable hydrogels with high drug loading through B–N coordination and ROS-triggered drug release for efficient treatment of chronic periodontitis in diabetic rats, *Biomaterials*, 2022, **282**, 121387.
 - 21 Z. Zhang, Q. Dou, S. Wang, D. Hu, B. Yang, Z. Zhao, H. Liu and Q. Dai, The development of an antifouling interpenetrating polymer network hydrogel film for salivary glucose monitoring, *Nanoscale*, 2020, **12**, 22787–22797.
 - 22 D. Li, K. Chen, H. Tang, S. Hu, L. Xin, X. Jing, Q. He, S. Wang, J. Song, L. Mei, R. D. Cannon, P. Ji, H. Wang and T. Chen, A Logic-Based Diagnostic and Therapeutic Hydrogel with Multistimuli Responsiveness to Orchestrate Diabetic Bone Regeneration, *Adv. Mater.*, 2022, **34**, e2108430.
 - 23 R. Liu, Q. Liang, J.-Q. Luo, Y.-X. Li, X. Zhang, K. Fan and J.-Z. Du, Ferritin-Based Nanocomposite Hydrogel Promotes Tumor Penetration and Enhances Cancer Chemoimmunotherapy, *Adv. Sci.*, 2024, **11**, 2305217.
 - 24 J. He, Z. Li, J. Wang, T. Li, J. Chen, X. Duan and B. Guo, Photothermal antibacterial antioxidant conductive self-healing hydrogel with nitric oxide release accelerates diabetic wound healing, *Composites, Part B*, 2023, **266**, 110985.
 - 25 W. E. G. Müller, M. Ackermann, S. Wang, M. Neufurth, R. Muñoz-Espí, Q. Feng, H. C. Schröder and X. Wang, Photothermal antibacterial antioxidant conductive self-healing hydrogel with nitric oxide release accelerates diabetic wound healing, *Cell. Mol. Life Sci.*, 2018, **75**, 21–32.
 - 26 K. Yang, X. Zhou, Z. Li, Z. Wang, Y. Luo, L. Deng and D. He, Ultrastretchable, Self-Healable, and Tissue-Adhesive Hydrogel Dressings Involving Nanoscale Tannic Acid/Ferric Ion Complexes for Combating Bacterial Infection and Promoting Wound Healing, *ACS Appl. Mater. Interfaces*, 2022, **14**, 43010–43025.
 - 27 H. Jafari, P. Ghaffari-bohlouli, D. Podstawczyk, L. Nie and A. Shavandi, Tannic acid post-treatment of enzymatically crosslinked chitosan-alginate hydrogels for biomedical applications, *Carbohydr. Polym.*, 2022, **295**, 119844.
 - 28 N. Ahmad, M. J. A. Al-Ghamdi, H. S. M. Alnajjad, B. B. A. Al Omar, M. F. Khan, Z. S. Almalki, A. A. Albassam, Z. Ullah, M. S. Khalid and K. Ashraf, A comparative brain Toxicopharmacokinetics study of a developed tannic acid nanoparticles in the treatment of epilepsy, *J. Drug Delivery Sci. Technol.*, 2022, **76**, 103772.
 - 29 H. Xia, Z. Dong, Q. Tang, R. Ding, Y. Bai, K. Zhou, L. Wu, L. Hao, Y. He, J. Yang, H. Mao and Z. Gu, Glycopeptide-Based Multifunctional Hydrogels Promote Diabetic Wound Healing through pH Regulation of Microenvironment, *Adv. Funct. Mater.*, 2023, **33**, 2215116.
 - 30 Y. Xiong, Z. Lin, P. Bu, T. Yu, Y. Endo, W. Zhou, Y. Sun, F. Cao, G. Dai, Y. Hu, L. Lu, L. Chen, P. Cheng, K. Zha, M.-A. Shahbazi, Q. Feng, B. Mi and G. Liu, A Whole-Course-Repair System Based on Neurogenesis-Angiogenesis Crosstalk and Macrophage Reprogramming Promotes Diabetic Wound Healing, *Adv. Mater.*, 2023, **35**, 2212300.